Quantitative phase-field modeling of two-phase solidification

R. Folch[1, 2] and M. Plapp[1]

[1]*Laboratoire de Physique de la Matière Condensée,*
CNRS/École Polytechnique, 91128 Palaiseau, France
[2]*Institut-Lorentz, Universiteit Leiden, Postbus 9506, 2300 RA Leiden, The Netherlands*[*]
(Dated: October 3, 2018)

A phase-field model that allows for quantitative simulations of low-speed eutectic and peritectic solidification under typical experimental conditions is developed. Its cornerstone is a smooth free-energy functional, specifically designed so that the stable solutions that connect any two phases are completely free of the third phase. For the simplest choice for this functional, the equations of motion for each of the two solid–liquid interfaces can be mapped to the standard phase-field model of single-phase solidification with its quartic double-well potential. By applying the thin-interface asymptotics and by extending the antitrapping current previously developed for this model, all spurious thin-interface corrections to the dynamics of the solid–liquid interfaces can be eliminated. This means that simulation results become independent of the thickness W of the diffuse interfaces. As a consequence, accurate results can be obtained using values of W much larger than the physical interface thickness, which yields a tremendous gain in computational power and makes simulations for realistic experimental parameters feasible. Convergence of the simulation outcome with decreasing W is explicitly demonstrated. Furthermore, the results are compared to a boundary-integral formulation of the corresponding free-boundary problem. Excellent agreement is found, except in the immediate vicinity of bifurcation points, a very sensitive situation where noticeable differences arise. These differences reveal that, in contrast to the standard assumptions of the free-boundary problem, out of equilibrium the diffuse trijunction region of the phase-field model can (i) slightly deviate from Young's law for the contact angles, and (ii) advance in a direction that forms a finite angle with the solid–solid interface at each instant. While the deviation (i) extrapolates to zero in the limit of vanishing interface thickness, the small angle in (ii) remains roughly constant, which indicates that it might be a genuine physical effect, present even for an atomic-scale interface thickness.

I. INTRODUCTION

The phase-field method has emerged in recent years as a powerful tool to study interface dynamics in areas such as solidification [1], solid–solid phase transformations [2], and fluid mechanics [3, 4]. Their common point is that the dynamics of interfaces is coupled to one or several transport fields, which can lead to the spontaneous emergence of complex interfacial patterns. The characteristic scale of such patterns is typically macroscopic, whereas the interfaces are rough on a scale of a few times the range of the interatomic forces. Because of this intrinsic scale separation, the evolution of pattern-forming interfaces has traditionally been formulated in terms of free-boundary problems (FBP), in which the interfaces are assimilated to mathematical surfaces without thickness [5]. However, the numerical treatment of FBPs is highly non-trivial, because one needs to discretize and track the sharp boundaries.

The phase-field method avoids this need by introducing additional fields to distinguish between phases. These "phase fields" take different, constant values in each bulk phase, and interpolate smoothly between these values through a diffuse interface of thickness W. The equations of motion for these auxiliary fields are set up so that one of their intermediate level sets, which will represent the interface, obeys the desired FBP in the so-called "sharp-interface limit", in which W tends to 0.

To construct these evolution equations, the physics of diffuse interfaces is typically used as a guide, and often some qualitative physical meaning can be attached to the phase field. In solidification, for instance, it can be interpreted as an order parameter, and its time evolution considered to be a relaxation towards the minimum of a free-energy functional, in the spirit of the time-dependent Ginzburg–Landau models for the out-of-equilibrium thermodynamics of phase transitions [6]. The sharp-interface limit of the model is then checked *a posteriori* by matching, order by order, terms of asymptotic expansions for the fields in powers of W in a region of slow (the bulk) and rapid (the interface) variation of the fields. At the lowest order in the interface thickness W, this procedure is quite straightforward and yields a FBP that does not exhibit a dependence on W.

[*]Present address: Max-Planck-Institut für Physik komplexer Systeme, Nöthnitzer Str. 38, 01187 Dresden, Germany

However, since the numerical discretization needs to resolve the rapid variation of the fields through the interfaces, simulations are only feasible using finite W. Furthermore, in order to reduce the gap between the scales of the interface thickness and the pattern, W often needs to be chosen several orders of magnitude thicker than in reality. It is therefore mandatory to assess the influence of W on the simulation results. This can be done rigorously by going to the next order in W in the above matching procedure. In this "thin-interface limit", in which W is small but finite, an effective FBP is obtained, which now generally contains terms that scale with W.

While these terms may reflect genuine (but small) physical effects associated with the thickness of the interfaces W, they have to be eliminated either by a judicious choice of the model and its parameters [7], or by additional terms in the evolution equations tailored to counterbalance these effects [4], or by a combination of both [8]. This is necessary to scale up W without altering appreciably the outcome of simulations. If all terms in W can be eliminated, the outcome is independent of W, at least below some value of W for which the effective FBP holds (and above which terms of higher order in W become important). This complete elimination was achieved for the first time by Karma and Rappel for the solidification of a pure substance with equal thermal diffusivities in both phases (symmetric model) [7]. Their pioneer work made it possible to quantitatively simulate dendritic growth in three dimensions [9]. More recently, the approach has been extended to the one-sided model, in which the diffusivity vanishes in the solid phase, the relevant case for alloy solidification [8].

Industrial alloys often have more than two components and more than one solid phase. As a first step to deal with such alloys, we formulate and test here a phase-field model that carries over the above advances to *two-phase* solidification, a problem that is both practically relevant in metallurgy and of interest for the physics of pattern formation: Eutectic and peritectic two-phase composite structures are, together with dendrites, the most common solidification microstructures found in industrial alloys [10]. At a binary eutectic or peritectic point, two different solid phases coexist with the liquid. Under certain conditions, both solids grow simultaneously in a cooperative manner (coupled growth). For eutectic alloys, the resulting composite can consist either of alternate lamellae of each solid phase or of rods of one phase immerged in a continuous matrix of the other.

Due to the presence of two different solid phases, coupled growth can exhibit a rich variety of different patterns. The best studied setting, used as a relevant example throughout this article, is the directional solidification of thin eutectic samples [11, 12, 13, 14, 15]. In this process, samples are pulled from a hot into a cold region with a constant velocity, and after a transient the solidification front reaches a steady state characterized by a fairly uniform lamellar spacing. This spacing is not intrinsically selected by the system, but depends on the growth history. Upon a (large enough) change of pulling velocity, the front undergoes various instabilities and exhibits many classical features of nonlinear physics, such as bifurcations to states of lower symmetry, periodic limit cycles, spatiotemporal chaos and soliton-like traveling perturbations [13, 14, 15, 16, 17].

Numerous phase-field models for two-phase or multi-phase solidification have been published [18, 19, 20, 21, 22, 23, 24, 25, 26, 27]. While such models can qualitatively [25, 26, 27] (or, in some cases, even quantitatively for some aspects [28]) reproduce experimental observations, more accurate modeling is necessary in order to carry out detailed comparisons to experiments on specific substances. Albeit all those previous models have the correct sharp-interface behavior, it seems quite difficult to perform a thin-interface analysis of them. As a consequence, the influence of the interface thickness on their results remains uncontrolled.

The reason for this difficulty is intricately linked to the construction of the models: The starting point for any asymptotic analysis is the equilibrium front solution that connects two different bulk phases. For a binary alloy, there are two or more fields involved (the composition and one or more phase fields) through two or more coupled nonlinear partial differential equations, generally without known analytic solution. In the sharp-interface limit $W \to 0$, the coupling between the equations tends to zero, so that a separate solution of each equation can be found and used in the asymptotic analysis; however, in the thin-interface limit (W small but finite), the coupling terms remain. A strategy to construct more tractable models is to choose the coupling terms such that they vanish in equilibrium, which obviously facilitates finding analytic equilibrium solutions for arbitrary coupling strength. Such a model has recently been developed for a dilute binary alloy [8].

For two-phase solidification, an additional difficulty arises, because one now needs to distinguish between more than two phases. The first phase-field models for eutectic growth used the standard solid–liquid phase field, and a concentration field [18, 19] or a second phase field [20, 21] to distinguish between the two solids, α and β. Again, the equilibrium front problem takes the form of at least two coupled nonlinear partial differential equations with no known analytic solution. Later on, it was proposed to assign a separate phase field p_i to each phase i, indicating its presence ($p_i = 1$) or absence ($p_i = 0$). Each phase field can then be understood as a local volume fraction, and $\sum_i p_i = 1$ locally [22]. If, on an interface that connects phases i and j, no other phase is present ($p_k = 0$, $k \neq i, j$), the above sum rule permits to eliminate one of the two remaining phase fields from the evolution equations, and the interface can be described by a single variable, which, again, makes the existence of an exact analytic solution more likely. However, the stable solution for the phase fields across an interface *does* typically present some amount of the other phase(s). Although this recalls the microscopic physical phenomenon of adsorption at an interface,

this effect has to be eliminated, because it would scale with the interface width. Recently, the use of the so-called double obstacle potential [29] in the volume fraction formulation [30] has permitted to reduce or even eliminate the presence of supplementary phases in the interfaces. In conjunction with the so-called interface-field method [31], this methodology has recently been applied to simulate eutectic growth [27]. However, no thin-interface analysis of such models is presently available, and might even be complicated by the singular nature of this free energy.

Having all this in mind, our strategy is to develop a phase-field model for two-phase solidification with a *smooth*, specifically designed free-energy functional that ensures the absence of third phases in the interfaces and with a coupling between the phase and concentration fields that vanishes in equilibrium. Although we use as a starting point a free-energy functional, we will not seek to link our model to explicit thermodynamic alloy models. Instead of this, the final goal is to simulate the given free-boundary problem (FBP) as efficiently as possible; the free energy functional is "engineered" in this perspective.

We obtain a model that can accommodate arbitrary eutectic or peritectic phase diagrams and that exactly reduces, for each of the two solid–liquid interfaces, to the standard phase-field model for the solidification into a single solid phase, with the standard quartic double-well potential. Obviously, this is advantageous, since we can build on the progress that has recently been made on this model [7, 8]. In particular, we extend to two-phase solidification the so-called "antitrapping current", a phenomenological addition to the phase-field equations that was recently introduced in order to achieve a quantitative phase-field formulation of alloy solidification [8]; more details will be given in Sec. III G.

We thoroughly test our model in two-dimensional simulations and compare the outcome to results obtained with the boundary integral method [17]. We find that the dynamics of the solid–liquid interfaces are accurately simulated and independent of the interface thickness for sufficiently thin interfaces, as predicted by the asymptotic analysis. However, the dynamics of trijunction points where the three interfaces meet differs from those traditionally postulated in the classic free-boundary formulation. These differences, due to the diffuseness of the trijunctions, are explored in detail in the numerical simulations (Sec. IV).

A preliminary account of some of our results has been given in Ref. [32]; here, we give a detailed presentation of both the model and the numerical simulations. The rest of the paper is structured as follows: We first recall the physics of eutectic solidification and write down the classic FBP (Sec. II). Next, we construct our phase-field model step by step (Sec. III); we explore the mapping to single-phase solidification on the solid–liquid interfaces to deduce their thin-interface behavior, and then refine the model to make this behavior match as closely as possible the FBP of Sec. II. In Sec. IV we present the numerical simulations and the lessons one can learn from them. We then conclude with a summary of our main results and a discussion of further prospects (Sec. V).

II.   FREE-BOUNDARY PROBLEM

Consider a binary, eutectic alloy. As a relevant example, we take the transparent organic mixture CBr_4–C_2Cl_6, for which accurate and extensive experimental data are available [13, 14, 15, 33]. Its phase diagram is shown in Fig. 1, where T is the temperature and C the composition, expressed as molar fraction of the solute, C_2Cl_6. The liquidus lines of two solid–liquid equilibria meet at the eutectic point (C_E, T_E), the lowest melting point of the alloy. At this temperature, liquid of composition C_E can coexist with two solids of composition $C_\alpha < C_E$ and $C_\beta > C_E$. These compositions define the limits of the eutectic plateau, of total width $\Delta C = C_\beta - C_\alpha$.

For slow solidification latent heat rejection can be neglected. The temperature is then constant throughout the system for isothermal boundary conditions (isothermal solidification). For directional solidification in an imposed thermal gradient, one must further assume equal heat conductivities in all phases for the temperature field to be independent of the interface position and fixed by the experimental setup only. For a gradient G directed along the z direction with pulling speed v_p in the negative z direction, we then have

$$T = T_E + G(z - v_p t), \tag{2.1}$$

where we have chosen the origin of the z axis at the position of the eutectic isotherm at $t = 0$.

The temperature of a solid–liquid interface is given by the generalized Gibbs-Thomson condition,

$$T = T_E + m_i(C_+ - C_E) - \frac{\sigma_{iL} T_E}{L_i}\kappa - \frac{v_n}{\mu_i} \tag{2.2}$$

where C_+, κ and v_n are the concentration on the liquid side of the interface, the local interface curvature, and its normal velocity, respectively, and $i = \alpha, \beta$. Up to the first two terms on its r.h.s., Equation (2.2) is the equation of the liquidus lines, where m_i are the liquidus slopes ($m_\alpha < 0$, $m_\beta > 0$), taken at the eutectic point, but assumed to be independent of the concentration. The third term on the r.h.s, where σ_{iL} are the solid–liquid surface tensions and
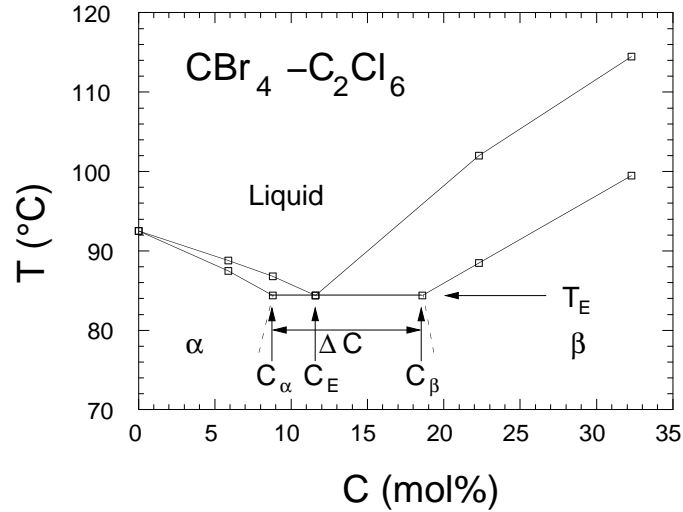
FIG. 1: Experimental phase diagram of the transparent organic eutectic alloy CBr$_4$–C$_2$Cl$_6$ (modified from J. Mergy, G. Faivre and S. Akamatsu). C is the concentration of C$_2$Cl$_6$, and we have indicated the eutectic temperature T_E, the equilibrium concentrations of each phase at the eutectic temperature, C_α, C_β, and C_E, and the width ΔC of the eutectic plateau.

L_i the latent heats of fusion per unit volume, represents the capillary effect which lowers the melting temperature of convex parts of the solid. Finally, the fourth term stands for the effects of interface kinetics; μ_i therein is the linear kinetic coefficient, defined as the proportionality constant between the local undercooling and the velocity of a flat interface. Eliminating the temperature between Eqs. (2.1) and (2.2), we obtain boundary conditions for the concentrations at an interface of specified position, velocity, and curvature [Eq. (2.5c) below].

Growth is limited by solute transport, much slower than that of heat. For solidification in thin samples, convection in the liquid is suppressed, and solute transport occurs by diffusion only. Furthermore, diffusion in the solid is in most cases so slow, that the final distribution of impurities is still the trace left by the concentration at the solid side of the solidification front C_-, which is assumed to follow the equilibrium partition relation

$$C_- = k_i C_+, \tag{2.3}$$

where k_i are the partition coefficients. Therefore, we neglect diffusion in the solid phases (one-sided model). Then, the velocity of the interface and the diffusion flux on the liquid side are related by the Stefan condition,

$$v_n(C_+ - C_-) = -\hat{n} \cdot (D\vec{\nabla}C|_+), \tag{2.4}$$

where $\hat{n}$ is the unit vector normal to the interface and pointing into the liquid. This condition expresses mass conservation: The concentration difference between the two phases has to be transported away by diffusion for the interface to move. As a corollary, in the one-sided model the solid–solid interfaces cannot move, and hence their shape is just the trajectory followed by the trijunctions.

All of the above already specifies the dynamics of each solid–liquid interface independently. Each of them is thus found to obey the following free-boundary problem:

$$\partial_t c = D\nabla^2 c \tag{2.5a}$$

$$D\hat{n} \cdot \vec{\nabla}c|_+ = [c_i - (1-k_i)c_+]v_n \tag{2.5b}$$

$$c_+ = \mp\left(\frac{z_{\text{int}} - v_p t}{l_T^i} + d_i\kappa + \beta_i v_n\right), \tag{2.5c}$$

where we have defined the scaled concentration field

$$c = \frac{C - C_E}{\Delta C} \tag{2.6}$$

and the scaled equilibrium concentrations of the two solids at the eutectic temperature,

$$c_i = \frac{C_i - C_E}{\Delta C}. \tag{2.7}$$

Equation (2.5a) holds in the liquid, and Equations (2.5b) and (2.5c) on the interface; the minus (plus) sign in Eq. (2.5c) is valid for the α–liquid (β–liquid) interface, z_{int} is the z position of the interface,

$$l_T^i = \frac{|m_i|\Delta C}{G} \tag{2.8}$$

are the thermal lengths,

$$d_i = \frac{\sigma_{i\text{L}} T_{\text{E}}}{L_i |m_i| \Delta C}, \tag{2.9}$$

the capillary lengths, and

$$\beta_i = \frac{1}{\mu_i |m_i| \Delta C}, \tag{2.10}$$

kinetic coefficients. We also define the average capillary and thermal lengths, $\bar{d} = (d_\alpha + d_\beta)/2$ and $\bar{l}_T = (l_T^\alpha + l_T^\beta)/2$, as well as the diffusion length

$$l_D = D/v_p. \tag{2.11}$$

Finally, the α–liquid and β–liquid interfaces are connected by imposing local equilibrium at trijunction points where three interfaces (α–liquid, β–liquid, and α–β) meet. The balance of the surface tension at the trijunction points reads

$$\hat{t}_{\alpha\text{L}}\sigma_{\alpha\text{L}} + \hat{t}_{\beta\text{L}}\sigma_{\beta\text{L}} + \hat{t}_{\alpha\beta}\sigma_{\alpha\beta} = \vec{0}, \tag{2.12}$$

where $\hat{t}_{ij}$ is a unit vector tangential to the i–j interface and pointing outwards from the trijunction. This condition, known as Young's law, yields the equilibrium angles between any two interfaces. An important special case is a steady-state composite structure such as the lamellae depicted in Fig. 2, for which the solid–solid interfaces are aligned with the z direction. The angles of the i–liquid interfaces with the x direction, called contact angles (we adopt the notation of Refs. [34, 35]), are given by the solution of the equations

$$\sigma_{\alpha\beta} = \sigma_{\alpha\text{L}} \sin\theta_\alpha + \sigma_{\beta\text{L}} \sin\theta_\beta \tag{2.13}$$
$$\sigma_{\alpha\text{L}} \cos\theta_\alpha = \sigma_{\beta\text{L}} \cos\theta_\beta. \tag{2.14}$$

For equal solid–liquid surface tensions, we have $\sin\theta_\alpha = \sin\theta_\beta = \sigma_{\alpha\beta}/(2\sigma_{i\text{L}})$.

Note that we have not taken into account crystallographic effects, which would appear through anisotropies in the kinetic coefficients and the surface tensions; the latter would also lead to additional "Herring torque" terms in Young's law. It has been shown by boundary integral simulations [16, 17] that all the relevant instabilities and morphologies can be reproduced by the above model. Therefore, we have limited ourselves to an isotropic formulation both for the FBP and the phase-field model.

The growth of lamellar composites has been analyzed in the seminal paper by Jackson and Hunt [36]. They found that there exists a family of steady-state solutions parameterized by the lamellar spacing λ (see Fig. 2). The average undercooling of the front, ΔT, depends on the spacing as

$$\Delta T = \frac{\Delta T_{\text{JH}}}{2} \left(\frac{\lambda}{\lambda_{\text{JH}}} + \frac{\lambda_{\text{JH}}}{\lambda} \right), \tag{2.15}$$

where

$$\Delta T_{\text{JH}} = \frac{2\sqrt{2}\Delta C}{\eta(1-\eta)} \left(\frac{m_\alpha m_\beta}{m_\alpha + m_\beta} \right) \sqrt{P(\eta)[(1-\eta)d_\alpha \sin\theta_\alpha + \eta d_\beta \sin\theta_\beta]/l_D} \tag{2.16}$$

$$\lambda_{\text{JH}} = \sqrt{2l_D[(1-\eta)d_\alpha \sin\theta_\alpha + \eta d_\beta \sin\theta_\beta]/P(\eta)}, \tag{2.17}$$

with $P(\eta) = \sum_{n=1}^{\infty} \sin^2(\pi\eta n)/(\pi n)^3$, and η the nominal volume fraction of the α phase at the eutectic temperature, related to the global sample composition c_∞ by $c_\infty = \eta c_\alpha + (1-\eta)c_\beta$ [34, 35, 36]. The front undercooling has a minimum ($\Delta T = \Delta T_{\text{JH}}$) for the spacing λ_{JH}, which constitutes a reference length for lamellar eutectics.
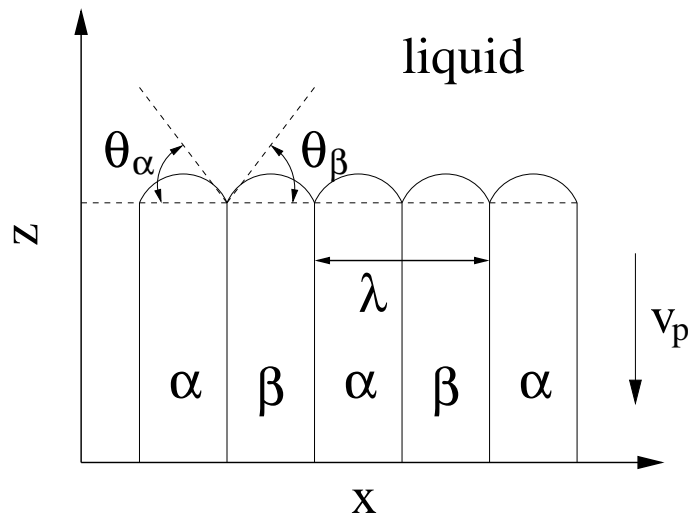
FIG. 2: Sketch of the lamellar geometry with the definitions of the contact angles θ_α and θ_β; η is the volume fraction of α phase, and λ the lamellar spacing.

III. PHASE-FIELD FORMULATION

In this section we construct and justify our phase-field model. We start by introducing our notation and a variational formulation (Sec. III A). Next, we introduce a free-energy functional that provides the minimal features of the model, i.e., three distinct phases with interfaces that are free of any adsorbed third phase, and enough freedom to fit a phase diagram (Sec. III B); The equilibrium properties of the model, including the phase diagram, are then verified in Sec. III C. The model is analyzed for a two-phase system, and it is found that it exactly reduces to the usual phase-field model of single-phase solidification (Sec. III D). This mapping allows us to deduce the thin-interface behavior of two-phase interfaces without performing a detailed asymptotic analysis. Furthermore, this analogy serves us as a guideline to extend the model, and, in particular, to allow for two independent kinetic coefficients on the two solid–liquid interfaces (Sec. III E), to introduce a non-variational formulation (Sec. III F), to address the one-sided case in which the solid diffusivity is neglected (Sec. III G), and the case of different surface tensions (Sec. III H).

Although we use as a starting point a free-energy functional, we should stress that we will not seek to link our model to an explicit thermodynamic formulation. The final goal is to obtain a model that simulates the free boundary problem of the previous section as efficiently as possible; the free-energy functional is "engineered" in this perspective.

A. Framework and notation

We use three phase fields p_i, $i = \alpha, \beta, \mathrm{L}$, and denote $\vec{p} \equiv (p_\alpha, p_\beta, p_\mathrm{L})$. Each field represents the volume fraction of a different phase, and hence we would like $p_i \in [0, 1] \, \forall i$ and

$$\sum_i p_i = 1. \tag{3.1}$$

We then introduce a free-energy functional

$$F = \int_V f \, dV, \tag{3.2}$$

defined as the volume integral of a free-energy density

$$f(\vec{p}, \vec{\nabla}\vec{p}, c, T) = K f_{\mathrm{grad}}(\vec{\nabla}\vec{p}) + H f_p(\vec{p}) + X f_c(\vec{p}, c, T), \tag{3.3}$$

whose dependencies have been broken down in the following way: f_p depends only on the phase fields and provides a "free-energy landscape" in $\vec{p}$; in particular, it contains the analog of the double-well potential of single-phase solidification. f_c couples the phase fields to concentration and temperature and hence defines the phase diagram. It does not contain a term in $(\vec{\nabla}c)^2$, which turns out to be unnecessary. Both f_p and f_c are dimensionless; H and

X are constants with dimensions of energy per unit volume. f_{grad} sets a free-energy cost for gradients in $\vec{p}$, forcing interfaces to have a finite width. We will use a quadratic form in the gradients of the phase fields, and thus generalize the squared-gradient term of single-phase solidification. Therefore, K has dimensions of energy per unit length.

In a variational formulation of the equations of motion, the non-conserved phase fields are assumed to evolve towards the minimum of F,

$$\tau(\vec{p})\frac{\partial p_i}{\partial t} = -\frac{1}{H}\left.\frac{\delta F}{\delta p_i}\right|_{p_\alpha+p_\beta+p_{\text{L}}=1} \qquad \forall i, \tag{3.4}$$

where H has been introduced on the right hand side to remove the dimensions of F, and $\tau(\vec{p})$ is a relaxation time that is the same in all Equations (3.4) (i.e., $\forall i$), but may depend on the local values of the phase fields (see Appendix A for a detailed motivation of this choice). The functional derivative has to be evaluated subject to the constraint of Eq. (3.1). This can be done by the method of Lagrange multipliers: A term $\xi(1 - \sum_j p_j)$ is added to the free-energy functional; the derivatives are taken as if the variables p_i were independent, and ξ is determined and eliminated. The result for three phases is

$$\left.\frac{\delta F}{\delta p_i}\right|_{p_\alpha+p_\beta+p_{\text{L}}=1} = \frac{\delta F}{\delta p_i} - \frac{1}{3}\sum_j \frac{\delta F}{\delta p_j}, \tag{3.5}$$

where the variations on the r.h.s. are now taken as if all p_i were independent. We recall that variations are evaluated according to

$$\frac{\delta F}{\delta p_i(\vec{x})} = \frac{\partial f}{\partial p_i} - \sum_\nu \partial_\nu \frac{\partial f}{\partial(\partial_\nu p_i)}, \tag{3.6}$$

where ν counts the spatial coordinates. Equations (3.4) and (3.5) automatically ensure $\sum_i \partial p_i/\partial t = 0$, which is necessary to maintain consistency with the constraint of Eq. (3.1). Note that we do not impose at this level $p_i \in [0,1]\,\forall i$, in contrast to other formulations [30]. This restriction will instead result from the specific design of our free-energy functional.

The concentration c is a conserved field, and thus obeys the continuity equation

$$\frac{\partial c}{\partial t} + \vec{\nabla}\cdot\vec{J} = 0, \tag{3.7}$$

where $\vec{J}$ is the flux of scaled concentration c,

$$\vec{J} = -M(\vec{p})\vec{\nabla}\frac{\delta F}{\delta c}, \tag{3.8}$$

with $M(\vec{p})$ a mobility.

As already mentioned in the introduction, the key point of our model is that an interface between any two phases i and j should be free of any adsorbed third phase, that is, $p_k \equiv 0\ \forall k \neq i,j$. If we construct a free-energy functional $\mathcal{F}$ such that $p_k = 0,1$ be the only homogeneous, stationary stable solutions of Eq. (3.4) for p_k, then a i–j interface will be free of phase k, since any perturbation around this solution would relax back to zero. More generally, this requirement will ensure that bulk phases $p_k = 1$ are stable, i–j interfaces are stabilized only by the presence of bulk phases i and j at each side and contain no third phase, triple junctions or lines can only exist where interfaces meet, and so on. Note also that, with appropriate initial and boundary conditions, this guarantees that $p_i \in [0,1]\,\forall i$ (for the continuum equations; in the discretized equations, small overshoots may occasionally appear). The requirements on $\mathcal{F}$ for stationarity and stability read respectively

$$\left.\frac{\delta F}{\delta p_k}\right|_{p_\alpha+p_\beta+p_{\text{L}}=1,\ p_k=0,1} = 0\ \ \forall k, \tag{3.9a}$$

$$\left.\frac{\delta^2 F}{\delta p_k^2}\right|_{p_\alpha+p_\beta+p_{\text{L}}=1,\ p_k=0,1} > 0\ \ \forall k. \tag{3.9b}$$

Furthermore, in order to ensure stability with respect to concentration fluctuations, we need to require

$$\frac{\delta^2 F}{\delta c^2} > 0, \tag{3.10}$$

which is just a standard condition of thermodynamic stability.

To construct a suitable free-energy functional, our strategy is to choose the two parts of the free-energy density that depend on the gradients only ($K f_{\text{grad}}$) and the local values of the fields only ($H f_p + X f_c$), respectively, such that the volume integral of each one separately satisfies the above conditions.

B.   Minimal model

For clarity of exposition, we first construct our model taking the parts of the free-energy density that functionally depend on the phase fields only, $f_{\mathrm{grad}}(\vec{\nabla}p)$ and $f_p(\vec{p})$, to be invariant under the exchange of any two phases. We will later break this symmetry in different ways as it becomes necessary.

For the energetic cost of the gradients of the phase fields, f_{grad}, we adopt the simplest scalar expression that is a regular and isotropic function of $\vec{\nabla}\vec{p}$ and respects this symmetry,

$$f_{\mathrm{grad}} = \frac{1}{2}\sum_i \left(\vec{\nabla}p_i\right)^2. \tag{3.11}$$

It is straightforward to check that the volume integral of this function satisfies Eqs. (3.9).

As for the potential part f_p, we take

$$f_p = f_{\mathrm{TW}}, \tag{3.12}$$

where the triple-well potential f_{TW} is the analog of the double well in the standard phase-field model of solidification with a single solid phase. In order to acquire some "geometric intuition" about its construction, it is useful to visualize it with the help of the Gibbs simplex. We recall (see also Appendix A) that the Gibbs simplex is an equilateral triangle of unit height, where each vertex represents a different phase (either α or β solid, or liquid), and, for any point, the (signed) distance to the side opposite to a given vertex represents the value of the phase field associated to that vertex. Thus, each side corresponds to a purely binary interface, and the center, $p_\alpha = p_\beta = p_{\mathrm{L}} = 1/3$, to the triple point. Points outside the triangle represent negative values of one or two phase fields.

The parts of the free-energy density that depend only on the local values of the fields, but not on their gradients, f_p and f_c, can be plotted as a surface over this simplex. Moreover, the conditions of Eqs. (3.9) on their volume integrals can be rewritten using Eq. (3.6) to replace functional with partial derivatives: Focusing on the part that we are now concerned with, $f_p = f_{\mathrm{grad}}$, the conditions read $\partial f_p/\partial p_k|_{p_\alpha+p_\beta+p_{\mathrm{L}}=1,\ p_k=0,1} = 0$ and $\partial^2 f_p/\partial p_k^2|_{p_\alpha+p_\beta+p_{\mathrm{L}}=1,\ p_k=0,1} > 0$. It can be easily verified that the left hand side of the first condition is equal to the slope of the f_p surface, plotted over the Gibbs simplex, in the direction k. Therefore, the conditions of Eqs. (3.9a) and (3.9b) can be understood as requiring zero slope (flatness) and convexity, respectively, in the direction normal to a side, both on that side and on the vertex opposite to it. In other words, the sides of the triangle must be valleys of the free-energy landscape, so that the stable solutions that connect two vertices run exactly along the sides (purely binary interfaces), and each vertex should be a local minimum; hence, there will necessarily be a saddle point on each side that will connect the two vertices of the side, and each interface will thus "feel" a double-well potential. There should be no other minimum.

The requirement for minima at $p_k = 0,1$ along the p_k direction [Eqs. (3.9)] suggests to construct the triple-well potential as a sum of equal double-well potentials $f_{\mathrm{DW}}(p)$ for all the phase fields:

$$f_{\mathrm{TW}} = \sum_i f_{\mathrm{DW}}(p_i). \tag{3.13}$$

If $f_{\mathrm{DW}}(p)$ has two equal minima at $p = 0,1$, f_{TW} will have equal global minima in each phase i characterized by $p_j = \delta_{ij}$. Applying the prescription of Eq. (3.5) for $p_k = 0,1$, we find that the slope is equal to $(2/3)(df_{\mathrm{DW}}/dp)(p = p_k) - (1/3)(df_{\mathrm{DW}}/dp)(p = p_i) - (1/3)(df_{\mathrm{DW}}/dp)(p = p_j)$. Since $p_k = 0,1$ and $(df_{\mathrm{DW}}/dp)(p = 0,1) = 0$, the first term is zero; furthermore, at $p_k = 1$ $p_i = p_j = 0$ and the other two terms vanish too; as for $p_k = 0$, then $p_j = 1 - p_i$, and it can be seen that flatness is satisfied whenever $f_{\mathrm{DW}}(1 - p) = f_{\mathrm{DW}}(p)$, i.e., if f_{DW} is even in $2p - 1$. Similarly, it can be shown that convexity is also satisfied as long as the double well convexity in the wells overcomes its concavity on the maximum in between, $2(d^2 f_{\mathrm{DW}}/dp^2)(p = 0,1) > -(d^2 f_{\mathrm{DW}}/dp^2)(p = 1/2)$. The standard quartic double well, proportional to

$$f_{\mathrm{DW}} = p^2(1 - p)^2, \tag{3.14}$$

satisfies the above requirements. This choice is particularly convenient since it will allow us to relate our model to the standard phase-field model. The result for f_{TW} is plotted in Fig. 3.

So far, all bulk phases correspond to equally deep wells, which means that they all have the same bulk free-energy density. However, the relative stability of phases generally depends on the local values of the concentration and the temperature. In the phase-field model for single-phase solidification, this is implemented by adding a function to the free-energy density that tilts the double well by an amount that is proportional to the local driving force for phase transformations. Here, we need to construct a function that tilts the triple well in such a way that the conditions of flatness (and, if possible, convexity), are maintained. Note that the condition of flatness in particular, Eq. (3.9a), not
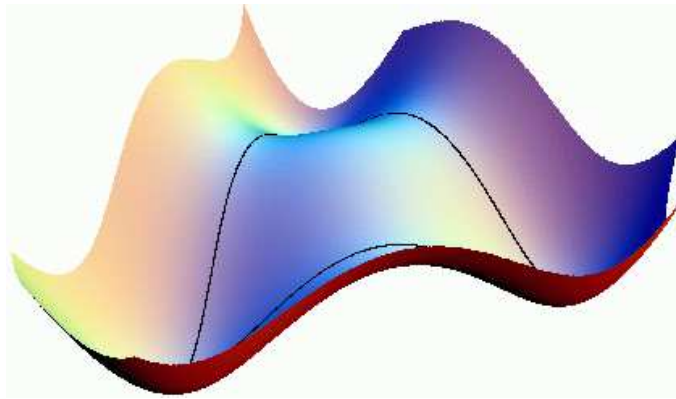
FIG. 3: Triple well potential, visualized as a surface over the Gibbs simplex. The black lines mark the borders of the Gibbs simplex, drawn on the surface; for this function, they also coincide with the trajectory of the equilibrium interface solutions.

only ensures the absence of third-phase adsorption, but also that the two wells of every pure i–j interface remain at $p_i = 0, 1$ in spite of the tilt, a condition known to be important for single-phase solidification [7].

We begin by constructing a function g_i which raises the well i, $g_i(p_i = 1) = 1$, and leaves the other two as well as the entire interface between them unaffected, $g_i(p_i = 0) = 0$. On the other two interfaces ($p_j = 0$ with $j \neq i$), we require g_i to be antisymmetric with respect to the saddle point of f_{TW} at $p_i = p_j = 1/2$, i.e.,

$$g_i(1 - p_i, p_i, 0) = 1 - g_i(p_i, 1 - p_i, 0). \tag{3.15}$$

This requirement is necessary to avoid undesirable thin-interface corrections in the matching to the free-boundary problem (see Refs. [8, 37]) and to adjust surface tensions independently of the phase diagram (see next subsection), and is hence important [38]. Replacing $1 - p_i$ by p_j and then exchanging the mute indices i and j, we can rewrite the requirement in the form

$$g_j(p_i, p_j, 0) = 1 - g_i(p_i, p_j, 0), \tag{3.16}$$

which can be understood as the analog of $p_j = 1 - p_i$ for $p_k = 0$. This latter form [Eq. (3.16)] will be used below. We also impose zero slope on all sides of the Gibbs simplex in accordance with Eq. (3.9a), but not convexity, for reasons which will soon become apparent.

The lowest-order polynomial in the phase fields that satisfies all the above requirements is fifth-order and unique at this order,

$$g_i = \frac{p_i^2}{4} \left\{ 15(1 - p_i) \left[1 + p_i - (p_k - p_j)^2 \right] + p_i \left(9p_i^2 - 5 \right) \right\}; \tag{3.17}$$

it is plotted in Fig. 4. Remarkably enough, this function reduces to the polynomial $p_i^3(10 - 15p_i + 6p_i^2)$ on the i–j and i–k interfaces when the constraint $p_i + p_j + p_k = 1$ is taken into account, which happens to be proportional to the tilting function used in the available quantitative models of single-phase solidification [7, 8].

We then couple the phase fields to the concentration c and the temperature T through the functions $g_i(\vec{p})$: We use these functions to interpolate between three free-energy parabolic wells in concentration

$$f_{c,i} = (c - A_i)^2/2 + B_i \tag{3.18}$$

for the three phases $i = \alpha, \beta, \mathrm{L}$, characterized by $p_j = g_j = \delta_{ij}$:

$$f_c = \frac{1}{2} \left[c - \sum_i A_i(T) g_i(\vec{p}) \right]^2 + \sum_i B_i(T) g_i(\vec{p}). \tag{3.19}$$

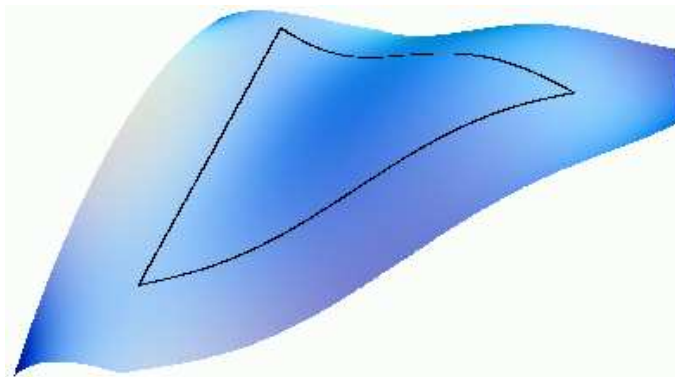The $A_i(T)$ and $B_i(T)$ define the equilibrium phase diagram, as discussed in the next subsection.

FIG. 4: Elementary tilting function g_i, visualized over the Gibbs simplex. The i vertex is to the right.

With f_c specified, we can now write down an explicit expression for the concentration current. We define a dimensionless chemical potential,

$$\mu = \frac{1}{X}\frac{\delta F}{\delta c} = \frac{\partial f_c}{\partial c} = c - \sum_i A_i(T)g_i(\vec{p}), \qquad (3.20)$$

so that Eq. (3.8) becomes

$$\vec{J} = -D(\vec{p})\vec{\nabla}\mu, \qquad (3.21)$$

where $D(\vec{p}) = M(\vec{p})X$ is a phase-dependent diffusivity. Note that the f_c in Eq. (3.19) or (3.20) satisfies the stability condition of Eq. (3.10).

Equation (3.9a) for no third-phase absorption also holds for f_c, since each of the g_i satisfies this condition by construction. However, no general statement can be made about the convexity of f_c, because it depends on the form of g_i and on the values of A_i, B_i and c. It can be shown that for special choices of the A_i and B_i, the second derivatives of f_c with respect to the third phase can be made to vanish throughout all borders of the Gibbs simplex. In any case, the other components of the free-energy density will ensure global convexity and hence stability for sufficiently small values of the ratio X/H. The solutions can always be stabilized by adding "obstacle" terms in the free energy, as discussed in Sec. III H below; however, our experience is that, whenever an instability occurs, the model is anyway too far from the thin-interface limit to represent the correct free-boundary problem, so that the convexity of f_c is not an issue in practice.

C. Equilibrium solutions

In order to illustrate how the evolution equations of the model are derived and to clarify the reasons for the particular choice of Eq. (3.19) for f_c, we derive the stationary solution for a planar interface. We check that this solution satisfies the conditions of thermodynamic equilibrium, compute its surface tension, and obtain the relationship between the coefficients $A_i(T)$ and $B_i(T)$ and the equilibrium phase diagram.

1. Evolution equations

We first write down explicitly the evolution equations for the minimal model, whose building blocks have been derived above. For the phase fields, we take the functional derivative of the free energy with respect to each phase field p_i according to Eq. (3.5), where the component of the free-energy density f_{grad} is given by Eq. (3.11), $f_p = f_{TW}$ by Eq. (3.13) with Eq. (3.14), and f_c by Eq. (3.19) with Eq. (3.17). Since c and μ are related, we can eliminate one

in order to reduce the number of variables; we choose to eliminate c. We obtain:

$$\tau(\vec{p})\frac{\partial p_i}{\partial t} = W^2\nabla^2 p_i + \frac{2}{3}\left[-2p_i(1-p_i)(1-2p_i) + \sum_{j\neq i}p_j(1-p_j)(1-2p_j)\right]$$

$$+ \tilde{\lambda}\sum_j \left.\frac{\partial g_j}{\partial p_i}\right|_{p_\alpha+p_\beta+p_{\mathrm{L}}=1}(\mu A_j - B_j) \quad \forall i, \tag{3.22}$$

$$\frac{\partial \mu}{\partial t} = \vec{\nabla}\cdot\left[D(\vec{p})\vec{\nabla}\mu\right] - \sum_i A_i\frac{\partial g_i(\vec{p})}{\partial t}, \tag{3.23}$$

where we have defined $W = \sqrt{K/H}$, $\tilde{\lambda} = X/H$, and

$$\left.\frac{\partial g_i}{\partial p_i}\right|_{p_\alpha+p_\beta+p_{\mathrm{L}}=1} = \frac{5}{2}p_i\left[(p_k - p_j)^2(3p_i - 2) + (1-p_i)^2(3p_i+2)\right], \quad i\neq j,k, \quad j\neq k, \tag{3.24}$$

$$\left.\frac{\partial g_j}{\partial p_i}\right|_{p_\alpha+p_\beta+p_{\mathrm{L}}=1} = -\frac{1}{2}\left.\frac{\partial g_i}{\partial p_i}\right|_{p_\alpha+p_\beta+p_{\mathrm{L}}=1} + \frac{15}{2}p_j^2(1-p_j)(p_k - p_i), \quad j\neq i, \quad k\neq i,j. \tag{3.25}$$

The evolution equation for μ is a diffusion equation with a source term that reflects the redistribution of solute at advancing interfaces.

Next, consider a generic i–j interface. Since we have taken care that our free-energy functional, if not all of its components, satisfies Eqs. (3.9) for $p_k = 0, 1$ ($k\neq i,j$), the phase field that corresponds to the third phase k vanishes, $p_k = 0$. Therefore, the sum rule of Eq. (3.1) can be used to eliminate p_j through $p_j = 1 - p_i$ [and hence g_j in terms of g_i, Eq. (3.16), $g_k(p_k = 0) = 0$], so that we are left with a single phase field p_i as desired. Equations (3.22–3.23) thus yield [39]

$$\tau(\vec{p})\frac{\partial p_i}{\partial t} = W^2\nabla^2 p_i - 2p_i(1-p_i)(1-2p_i)$$

$$- 15\tilde{\lambda}p_i^2(1-p_i)^2\left[\mu\left(A_j - A_i\right) - (B_j - B_i)\right] \tag{3.26}$$

$$\frac{\partial \mu}{\partial t} = \vec{\nabla}\cdot\left[D(\vec{p})\vec{\nabla}\mu\right] + (A_j - A_i)\frac{\partial g_i(p_k = 0)}{\partial t}, \tag{3.27}$$

where $g_i(p_k = 0)$ is evaluated using $p_j = 1 - p_i$.

2. Stationary solutions

We search for stationary planar interface solutions of Eqs. (3.26) and (3.27), that is, solutions that have vanishing time derivatives but vary in space along a single coordinate x and connect bulk phases i [$p_i(x = -\infty) = 1$] and j [$p_i(x = +\infty) = 0$]. From the condition $\partial\mu/\partial t = 0$ we obtain that the chemical potential μ, if bounded, has to be a constant in space. This is of course one of the conditions of thermodynamic equilibrium, and we hence denote this constant by μ_{eq}^{ij}. Its value is fixed by the second requirement, $\partial p_i/\partial t = 0$, through a solvability condition for the stationary, one-dimensional version of Eq. (3.26),

$$W^2\partial_{xx}p_i = 2p_i(1-p_i)(1-2p_i) + 15\tilde{\lambda}p_i^2(1-p_i)^2\left[\mu\left(A_j - A_i\right) - (B_j - B_i)\right] = -\frac{dV(p_i)}{dp_i}, \tag{3.28}$$

where the second equality defines a "potential" $V(p_i) = -p_i^2(1-p_i)^2 - (\tilde{\lambda}/2)p_i^3(10 - 15p_i + 6p_i^2)\left[\mu\left(A_j - A_i\right) - (B_j - B_i)\right]$ up to a constant. This notation refers to the well-known "particle-on-a-hill" analogy, in which Eq. (3.28) is interpreted as an equation of motion with time coordinate x for a point particle of position p_i that moves in the potential V. Since there is no dissipative term, a solution to this equation that connects $p_i = 0$ and $p_i = 1$ exists if and only if $V(0) = V(1)$, which requires the squared bracket $\left[\mu\left(A_j - A_i\right) - (B_j - B_i)\right]$ to vanish and hence yields

$$\mu_{\mathrm{eq}}^{ij}(T) = \frac{B_j(T) - B_i(T)}{A_j(T) - A_i(T)}. \tag{3.29}$$

The phase-field profile obtained with the remaining term of Eq. (3.28) and the given boundary conditions reads

$$p_i(x) = \frac{1}{2}\left[1 - \tanh\left(\frac{x - x_0}{\sqrt{2}W}\right)\right], \tag{3.30}$$

the desired solution for an interface centered on x_0. Equations (3.29) and (3.30) together with the definition of μ [Eq. (3.20)] and the condition $\mu = \mu_{\text{eq}}^{ij}$ determine the concentration profile,

$$c(x) = \mu_{\text{eq}}^{ij} + A_i g_i[\vec{p}(x)] + A_j g_j[\vec{p}(x)]. \tag{3.31}$$

Taking the limits $x \to \pm\infty$, we find the concentration of phase i in equilibrium with phase j,

$$c_i^{ij} = A_i + \frac{B_j - B_i}{A_j - A_i}. \tag{3.32}$$

By choosing appropriate functions $A_i(T)$ and $B_i(T)$, we can reproduce any phase diagram as characterized by its coexistence lines $c_i^{ij}(T)$. Since only free energy or concentration differences between phases are relevant [note the form of the square bracket in Eqs. (3.26) or (3.28)], we may choose $A_{\text{L}} = B_{\text{L}} = 0$ without loss of generality. With the remaining four functions of T we can fit two liquidus and two solidus lines; the solid–solid equilibrium is then constrained, but this is irrelevant for the one-sided case, for which the solid has no dynamics.

3. Relation to thermodynamics

To obtain the thermodynamic interpretation of the above solvability condition $V(0) = V(1)$, note that the two terms in the middle of Eq. (3.28) correspond to $(1/2)(d/dp_i)f_p(p_i, 1 - p_i, 0)$ and $(1/2)\tilde{\lambda}(\partial/\partial p_i)f_c(p_i, 1 - p_i, 0)$, respectively [39]. The second is a partial derivative because f_c also depends on p_i implicitly through $c(p_i)$ [Eq. (3.31)]; its total derivative is $(d/dp_i)f_c = (\partial/\partial p_i)f_c + (\partial f_c/\partial c)(dc/dp_i)$, where $\partial f_c/\partial c = \mu$ is the constant μ_{eq}^{ij} in equilibrium. Therefore, this second term can also be written as $(1/2)\tilde{\lambda}(d/dp_i)(f_c - \mu c)$. By formal integration of the second equality in Eq. (3.28) we thus obtain (for constant μ)

$$V(p_i) = -\frac{1}{2}\left\{f_p(p_i, 1 - p_i, 0) + \tilde{\lambda}\left[f_c(p_i, 1 - p_i, 0, c) - \mu_{\text{eq}}^{ij}c\right]\right\} \tag{3.33}$$

up to a constant, to be compared to the (dimensional) grand potential density,

$$\omega = f - X\mu c = K f_{\text{grad}} + H f_p + X(f_c - \mu c) = K f_{\text{grad}} - 2HV(p_i), \tag{3.34}$$

where the last equality holds for constant μ and we recall that $\tilde{\lambda} = X/H$. Since f_{grad} vanishes in bulk phases, the condition $V(0) = V(1)$ implies that the grand potential density be equal in the two coexisting phases, $\omega(0) = \omega(1) = \omega_{\text{eq}}^{ij}$. We hence see that the two conditions for the existence of a stationary solution correspond to equality of chemical and grand potentials. Since f_p takes the same value in all bulk phases, we note that the equality of grand potentials simply requires that of $f_c - \mu c$. The latter, together with a constant $\mu = \partial f_c/\partial c$, is what is usually represented graphically in the well-known common tangent construction, illustrated in Fig. 5.

4. Surface tension and choice of f_c

At this point, it is important to realize that the conditions of stationarity, or, equivalently, the common tangent construction, only require the grand potential ω and the quantity $f_c - \mu c$ to take equal values *at both sides* of the interface. However, they both generally vary *through* it, which means that their surface excesses are typically finite. The surface excess of the grand potential, for instance, gives the surface tension,

$$\sigma_{ij} = \int_{-\infty}^{+\infty} \{\omega[\vec{p}(x), c(x)] - \omega_{\text{eq}}^{ij}\}dx. \tag{3.35}$$

The particularity of our model can now be understood: At equilibrium, $\mu = \mu_{\text{eq}}^{ij}$ happens to make the square brackets and hence the whole term proportional to $\tilde{\lambda}$ in Eq. (3.28) vanish for any value of p_i, i.e., throughout the whole interface. This decouples the phase and chemical potential fields at equilibrium, as emphasized in the introduction. More
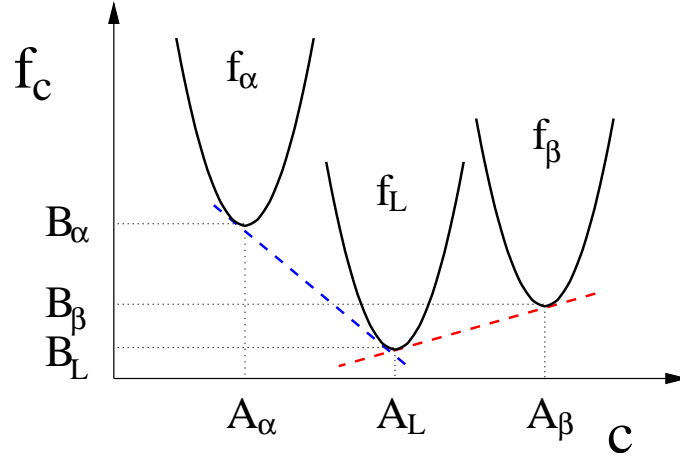
FIG. 5: The f_c part of the free-energy density is an interpolation between three parabolic bulk phase free energies; the equilibrium compositions and chemical potentials can be obtained by the common tangent construction illustrated by the straight, dashed lines for both solid–liquid equilibria. This construction corresponds to the conditions of equal chemical and grand potential in the two coexisting phases.

precisely, the equilibrium phase-field profile [Eq.(3.30)] balances the derivatives of Kf_{grad} and Hf_p only; moreover, since we saw that the term proportional to $\tilde{\lambda}$ corresponds to $(1/2)\tilde{\lambda}(\partial/\partial p_i)f_c(p_i, 1-p_i, 0) = (1/2)\tilde{\lambda}(d/dp_i)(f_c - \mu c)$, the fact that it vanishes means that $f_c - \mu c$ is constant throughout the interface, i.e., it has no surface excess. Therefore, it does not contribute to the surface tension, which again is determined purely by the remaining $Kf_{\mathrm{grad}} + Hf_p$. We obtain

$$\sigma_{ij} = \frac{\sqrt{2}}{3}\sqrt{KH} = \frac{\sqrt{2}}{3}\,WH. \tag{3.36}$$

To better realize the importance of this point, it is useful to consider the roles of the coefficients K, H and X in the free energy. X is the dimensional prefactor of the concentration-dependent terms and hence sets the magnitude of the thermodynamic driving forces, which is a macroscopic, physically measurable quantity. In contrast, K and H can be adjusted in order to achieve a desired surface tension and interface thickness. In our model, this is particularly straightforward since σ_{ij} does not depend on X: The interface thickness W can be varied for computational convenience while keeping the measured value for σ_{ij} just by fitting H [see Eq. (3.36)], and, still, X can be chosen independently to match its measured value. The capillary lengths d_i are proportional to the ratio of the surface tension to the driving forces ($d_i \propto \sigma_{i\mathrm{L}}/X$). Since $\sigma_{ij} \propto WH$, $d_i \propto WH/X = W/\tilde{\lambda}$, a scaling that will be confirmed by the thin-interface analysis given in the next subsection. This means that scaling up simultaneously W and $\tilde{\lambda}$ will leave the physics invariant, as desired.

For a generic model, in contrast, the terms proportional to $\tilde{\lambda}$ do *not* vanish in the equation of motion for p_i nor in the expression for the grand potential. Therefore, the phase and chemical potential fields do not decouple; both the phase-field profile (and therefore its thickness W) and the surface tension depend on the three constants K, H, and X, and no general analytic solution exists. In the expression for the surface tension, there is an extra contribution coming from f_c, which, on dimensional grounds, should be proportional to WX. Therefore, changing W while keeping the surface tension and driving forces fixed is far more complicated. Furthermore, the coupling to f_c will introduce some dependence of the surface tension and capillary lengths on the composition and temperature. While such dependencies may reflect some physical effects, it is difficult to control them properly since they will be blown up as the interface thickness W is scaled up to allow for simulations.

The advantage of our model comes from the fact that the partial derivative of f_c with respect to any of the two phase fields present on an interface, $(\partial f_c/\partial p_i)|_{p_\alpha + p_\beta + p_\mathrm{L} = 1, p_k = 0}$, vanishes at equilibrium *for any value of p_i*, i.e., thanks to the particular f_c used. More specifically, we achieve this through an f_c whose partial derivative splits in (i) a factor which depends on p_i only and (ii) one which depends on μ only, but none on c. In turn, for the particular type of polynomial construction of f_c we use, (i) can be traced back to the symmetry of the g_i's [Eq. (3.16)], and (ii) to the fact that the second derivatives of the bulk-phase free energies with respect to concentration are constant and all equal. The symmetry of the g_i's can be understood physically as ensuring that f_c depends only on relative differences

of free energy and concentration between any pair of phases i and j, *for any phase fraction* of the two phases p_i and $1 - p_i$. This is reflected in the expression in square brackets in Eqs. (3.26) or (3.28). Apart from this symmetry, the g_i are arbitrary, phenomenological phase-field interpolation functions.

In contrast, the free energies of the different bulk phases are, in principle, functions that are fixed for a given alloy system and cannot be freely adjusted. Our free energy is therefore an approximation, justified by the fact that it yields the desired phase diagram. However, apart from the phase diagram, the free energy also determines the latent heats, as we shall outline below, and these enter the capillary lengths [Eq. (2.9)]; moreover, due to the Gibbs-Thomson effect or to kinetics, the concentrations at both sides of a solid–liquid interface can deviate from the prediction of the phase diagram at a given temperature, which affects the amount of impurity actually rejected. As we shall see, our approximation for f_c constraints the capillary lengths and slightly modifies the impurity redistribution; however, the first is compatible with the experimentally measured values, and the second is completely negligible for low-speed solidification. To get rid of this approximation, it should be possible to use an approach recently introduced for dilute alloys in which internal energy and entropy are interpolated by two different functions [8]. However, the generalization of this method to two-phase solidification, that is, the introduction of two different sets of g_i functions, is outside the scope of the present paper.

D. Mapping of each solid–liquid interface to single-phase solidification

Here, we address the behavior of our model for small but finite values of the interface thickness W. It would be very interesting to investigate this behavior including the triple junctions; however, the problem there is quite involved, since two independent phase fields and the chemical potential vary rapidly and are all coupled. Therefore, we limit ourselves to an analysis of the interfaces, taking advantage of a mapping to single-phase solidification. The behavior of the trijunction points will be investigated numerically and discussed in detail in Sec. IV.

We are actually interested in solid–liquid interfaces, since the solid–solid one has no dynamics. We hence set $j = \mathrm{L}$ in Eqs. (3.26) and (3.27). To proceed, we rewrite the expression $\mu(A_\mathrm{L} - A_i) - (B_\mathrm{L} - B_i)$ thus appearing in Eq. (3.26) as $(A_\mathrm{L} - A_i)(\mu - \mu_\mathrm{eq}^{i\mathrm{L}})$, where $\mu_\mathrm{eq}^{i\mathrm{L}} = (B_\mathrm{L} - B_i)/(A_\mathrm{L} - A_i)$ is the dimensionless chemical potential for coexistence of the solid i and the liquid as given by Eq. (3.29)]. It hence becomes apparent that the driving force, $-15\tilde{\lambda}p_i^2(1 - p_i)^2(A_\mathrm{L} - A_i)(\mu - \mu_\mathrm{eq}^{i\mathrm{L}})$, is proportional to a deviation from equilibrium. Let us first consider isothermal solidification, so that $A_i(T)$, $A_\mathrm{L}(T)$ and $\mu_\mathrm{eq}^{i\mathrm{L}}(T)$ are just constants. Then, the evolution equations can we rewritten in terms of a new variable

$$u = (\mu - \mu_\mathrm{eq}^{i\mathrm{L}})/(A_\mathrm{L} - A_i), \tag{3.37}$$

which measures departure from equilibrium on the i–L interface, and a new phase field $\phi_i \equiv 2p_i - 1$, which takes the values $+1$ and -1 in the i solid and liquid phases, respectively. We obtain:

$$\tau(\vec{p})\frac{\partial \phi_i}{\partial t} = W^2\nabla^2\phi_i + \phi_i(1 - \phi_i^2) - \frac{15}{8}(A_\mathrm{L} - A_i)^2\tilde{\lambda}(1 - \phi_i^2)^2 u \tag{3.38}$$

$$\frac{\partial u}{\partial t} = \vec{\nabla} \cdot \left[D(\vec{p})\vec{\nabla}u\right] + \frac{\partial g_i(p_j = 0)}{\partial t}, \tag{3.39}$$

where j denotes the other (absent) solid phase.

With a constant relaxation time, $\tau(\vec{p}) \equiv \tau_0$, and a constant diffusivity, $D(\vec{p}) \equiv D$, the above equations constitute precisely the phase-field model for the solidification of a pure substance treated by Karma and Rappel, if the combination $(15/8)(A_\mathrm{L} - A_i)^2\tilde{\lambda}$ is identified with the coupling constant λ used in Ref. [7]; more precisely, we recover the variational version of their model. Therefore, we can use their results on its thin-interface behavior, i.e., the behavior for values of W much smaller than a typical lengthscale of the microstructural pattern. This is described by an effective free boundary problem for the field u. Undoing the change of variables of Eq. (3.37) and applying Eq. (3.20), we can compare it with the desired free-boundary problem of Eqs. (2.5):

We find that the Gibbs-Thomson boundary condition, Eq. (2.5c), is satisfied, with capillary lengths and kinetic coefficients related to the phase-field parameters by

$$d_i = a_1\frac{W}{|A_\mathrm{L} - A_i|\tilde{\lambda}}, \tag{3.40}$$

$$\beta_i = a_1\left[\frac{\tau_0}{|A_\mathrm{L} - A_i|\tilde{\lambda}W} - a_2|A_\mathrm{L} - A_i|\frac{W}{D}\right], \tag{3.41}$$

where $a_1 = \sqrt{2}/3$ and $a_2 = 0.7464$ are numerical constants related, but not equal to [40] those in Ref. [7]. We note that, in general, the expressions for the capillary lengths and the kinetic coefficients are not the same for the

two solid–liquid interfaces, but depend on the A_i's, and hence on concentration differences [recall Eq. (3.19)]. As anticipated, the parameter $\tilde\lambda$ controls the ratio of the interface thickness W to the smallest physical lengthscales, the capillary lengths d_i. The former can be varied while keeping the latter fixed just by changing $\tilde\lambda$ accordingly. For quantitative output, the simulation results should hence become independent of $\tilde\lambda$ for $\tilde\lambda$ small enough. This will be checked for our model in Sec. IV. Note that, as discussed in detail in Refs. [7, 8], convergence may be achieved for $\tilde\lambda$ much larger than 1, since it is only assumed that W is much smaller than a typical length scale of the pattern, which, in turn, is usually much larger than d_i.

The diffusion equation, Eq. (2.5a), is also satisfied. As for the mass conservation condition, we find

$$D\hat n \cdot (\vec\nabla c|_+ - \vec\nabla c|_-) = (A_i - A_{\mathrm L})v_n, \tag{3.42}$$

where $\vec\nabla c|_+$ and $\vec\nabla c|_-$ denote the concentration gradients on the liquid $(+)$ and the solid $(-)$ side of the interface, respectively. There are two differences with the Stefan condition of the desired FBP, Eq. (2.5b). Obviously, in the one-sided case the diffusion flux on the solid side vanishes, and hence the second term on the left hand side is absent. We address this case in Sec. III G. But there is a second difference: The right hand side of Eq. (3.42) corresponds to the right hand side of Eq. (2.5b) only for constant concentration gaps, $k_i = 1$. To see this, substitute Eq. (2.2), absorbing its temperature dependence in the phase-diagram concentration gaps $c_i^{i\mathrm L} - c_{\mathrm L}^{i\mathrm L}$, into Eq. (2.5b). This yields $D\hat n \cdot \vec\nabla c = v_n \left[c_i^{i\mathrm L} - c_{\mathrm L}^{i\mathrm L} \pm (1 - k_i)(d_i\kappa + \beta_i v_n)\right]$. The term $c_i^{i\mathrm L} - c_{\mathrm L}^{i\mathrm L}$ corresponds to our $A_i - A_{\mathrm L}$ [see Eq. (3.32)], but the other terms are lacking. This is due to the use of equal $\partial^2 f_{c,i}/\partial c^2$ for all three bulk-phase free-energy functions $f_{c,i}$ [Eq. (3.18)], as announced in Sec. III C: When the chemical potential is shifted from its temperature-dependent equilibrium value for a flat interface, the corresponding shifts in concentration are determined by $\partial\mu/\partial c = \partial^2 f_c/\partial c^2$ and are hence the same at both sides of each solid–liquid interface. This explains why our model displays the right deviations of c from its phase-diagram value at the liquid side [correct Gibbs-Thomson condition, Eq. (2.5c)], but does not reflect them in the concentration gaps that appear in the impurity rejection. However, the magnitude of the missing terms is small, since the departure from the equilibrium phase diagram is very small in slow solidification: The $\beta_i v_n$ term is usually neglected and will be set to zero in our simulations; as for $d_i\kappa$, a typical curvature κ is given by the inverse of the lengthscale of the microstructural pattern. In turn, this lengthscale goes as $\sqrt{\bar d l_D}$, where $l_D = D/V_p$ is the diffusion length. Therefore, $d_i\kappa \sim \sqrt{\bar d/l_D}$. For typical experimental values of slow solidification $\bar d/l_D \sim 10^{-4} - 10^{-5}$, so this correction can be safely neglected.

The other constraint coming from the equal $\partial^2 f_{c,i}/\partial c^2$ is reflected in Eq. (3.40): The ratio of the capillary lengths is fixed to

$$\frac{d_\alpha}{d_\beta} = \frac{|A_\beta - A_{\mathrm L}|}{|A_\alpha - A_{\mathrm L}|}. \tag{3.43}$$

This relation can be understood from thermodynamic considerations: The latent heats of the two solid–liquid phase transformation can be evaluated from the bulk-phase free energies f_i of [Eq. (3.18)] by $L_i = T(s_{\mathrm L} - s_i)$, where $s_i = -(\partial f_i/\partial T)|_c$ is the specific entropy of phase i (and similarly for the liquid). Making use of the conditions of equal chemical potential and grand potentials, we find $L_i = (\partial\mu_{\mathrm{eq}}^{i\mathrm L}/\partial T)|_c(c_i^{i\mathrm L} - c_{\mathrm L}^{i\mathrm L}) = (\partial\mu_{\mathrm{eq}}^{i\mathrm L}/\partial c)|c_i^{i\mathrm L} - c_{\mathrm L}^{i\mathrm L}|/m_i$. Since for both solid–liquid equilibria $(\partial\mu_{\mathrm{eq}}^{i\mathrm L}/\partial c) = \partial^2 f_c/\partial c^2|_{\mathrm{eq}}$ are the same, we find $L_\alpha/L_\beta = |(c_\alpha^{\alpha\mathrm L} - c_{\mathrm L}^{\alpha\mathrm L})/(c_\beta^{\beta\mathrm L} - c_{\mathrm L}^{\beta\mathrm L})|(m_\beta/m_\alpha)$. Using the definition of the capillary lengths, Eq. (2.9), this yields

$$\frac{d_\alpha}{d_\beta} = \frac{\sigma_{\alpha\mathrm L}}{\sigma_{\beta\mathrm L}}\left|\frac{c_\beta^{\beta\mathrm L} - c_{\mathrm L}^{\beta\mathrm L}}{c_\alpha^{\alpha\mathrm L} - c_{\mathrm L}^{\alpha\mathrm L}}\right| = \frac{\sigma_{\alpha\mathrm L}}{\sigma_{\beta\mathrm L}}\left|\frac{A_\beta - A_{\mathrm L}}{A_\alpha - A_{\mathrm L}}\right|, \tag{3.44}$$

where the second equality makes use of Eq. (3.32). Since, in our minimal model, $\sigma_{\alpha\mathrm L} = \sigma_{\beta\mathrm L}$, Eq. (3.43) follows. In general, the ratio depends on the temperature through the $c_i^{ij}(T)$. Near the eutectic point where solidification occurs for small undercoolings,

$$\frac{d_\alpha}{d_\beta} \approx \frac{\sigma_{\alpha\mathrm L}}{\sigma_{\beta\mathrm L}}\left|\frac{c_\beta}{c_\alpha}\right|. \tag{3.45}$$

This latter relation is satisfied by the reference alloy of our present study, CBr_4–C_2Cl_6, to within experimental accuracy.

Note that these lacking terms in the solute rejection and the restriction on the ratio of the capillary lengths do not vary with the interface thickness, but are zeroth-order corrections: They are not introduced by the diffuseness of the interfaces, but by our approximation for the free energy, which can be replaced by more sophisticated choices if needed, as already discussed at the end of Sec. III C 4.

Let us conclude this section with a comment on directional solidification, where the assumption of constant $A_i(T)$ and $A_{\mathrm{L}}(T)$ is no longer valid. If we still want to apply the mapping to single-phase solidification, we must neglect the temperature variation of $A_i(T)$ and $A_{\mathrm{L}}(T)$ within the region where the mapping holds. The scale of variation of the temperature is set by the thermal lengths l_T^i defined in Sec. II, whereas the mapping region needs to extend over at least a few times W in order for the thin-interface behavior of the model to be well defined (and the results of Ref. [7] to apply). Because these results already assume that the lengthscale of the pattern is much larger than W, and taking into account that the thermal lengths are typically far larger than this pattern lengthscale, the condition $W \ll l_T^i$ is automatically met. Therefore, even in presence of a temperature gradient, the results of Eqs. (3.40) and (3.41) apply, with the value of T (and hence $A_i(T)$ and $A_{\mathrm{L}}(T)$) taken in the center of the interface.

E. Independent kinetic coefficients

The relation between the phase-field parameters τ_0, $\tilde{\lambda}$ and W and the interface kinetic coefficients of the FBP is given by Eq. (3.41), where $|A_{\mathrm{L}} - A_i| = |c_{\mathrm{L}}^{i\mathrm{L}} - c_i^{i\mathrm{L}}|$ are set by the phase diagram, D is a material parameter, and a_1 and a_2 are numerical constants. Given a desired accuracy as fixed by W or, equivalently, $\tilde{\lambda}$ [linked by Eq. (3.40)], the only free parameter left is the phase-field relaxation time τ_0. However, we need at least two free parameters in the model, since there are two kinetic coefficients that are *a priori* independent. In the formulation of Ref. ([31]) with a double-obstacle potential, this is implemented by specifying different relaxation times τ_{ij} for each binary (i–j) phase transformation. In our formulation with a smooth free energy functional, this is not possible, as shown in Appendix A. Instead, we achieve independent kinetic coefficients by keeping the same relaxation time τ for all possible transformations, *but* making τ dependent on the phase fields.

In order to maintain the mapping to the model of Ref. [7] on the individual interfaces, τ has to be a constant along those interfaces. A function taking different, constant values on all three interfaces necessarily has discontinuity lines inside the Gibbs simplex. Here, we are mainly interested in controlling the dynamics of the solid–liquid interfaces, since, in the final one-sided model, the solid–solid interface does not move. Therefore, we use a function that takes constant values (τ_α and τ_β) on the two solid–liquid interfaces only, and interpolates smoothly between them *inside* the Gibbs simplex:

$$\tau(\vec{p}) = \begin{cases} \bar{\tau} + \frac{\tau_\beta - \tau_\alpha}{2} \frac{(p_\beta - p_\alpha)}{(p_\alpha + p_\beta)} & \text{if } p_{\mathrm{L}} \neq 1 \\ \bar{\tau} & \text{if } p_{\mathrm{L}} = 1, \end{cases} \tag{3.46}$$

where $\bar{\tau} = (\tau_\alpha + \tau_\beta)/2$. Note that the only discontinuity is on the vertex $p_{\mathrm{L}} = 1$. It did not cause any problems in practice, but, if needed, it could be smoothed out in a small neighborhood of the vertex without inducing appreciable errors in the calculations.

As a result of this procedure, the two kinetic coefficients,

$$\beta_i = a_1 \left[\frac{\tau_i}{|A_{\mathrm{L}} - A_i| \tilde{\lambda} W} - a_2 |A_{\mathrm{L}} - A_i| \frac{W}{D} \right], \tag{3.47}$$

can now be adjusted independently by choosing the two constants τ_α and τ_β.

F. Non-variational model

It has been shown for phase-field models of single-phase solidification [7, 37] that it is often advantageous to introduce an additional degree of freedom by switching to a non-variational formulation, which exploits the two different roles of the tilting functions g_i: In the evolution equations for the phase fields, Eq. (3.22), they favor one bulk phase over the other; in the one for the chemical potential μ, Eq. (3.23), they constitute a source or sink of μ, which corresponds to impurity rejection or adsorption, respectively. The g_i need to satisfy certain common requirements for both of their roles (although for different reasons), namely to interpolate from 0 to 1 as p_i goes from 0 to 1 and to be antisymmetric with respect to the point $p_i = p_j = 1/2$ on i–j interfaces [Eq. (3.15)]. However, the requirement of flatness, Eq. (3.9a), constrains only the derivatives with respect to the phase fields, which do not enter the evolution equation of the chemical potential μ.

Therefore, we can switch to a different chemical-potential-like variable,

$$\mu = c - \sum_i A_i h_i(\vec{p}), \tag{3.48}$$

which amounts to replace the g_i in Eq. (3.20) by new functions h_i that have the same limits and symmetries as the g_i, but do not necessarily satisfy Eq. (3.9a). This implies that the $\partial_t g_i$ in Eq. (3.23) are replaced by $\partial_t h_i$. Furthermore, a different expression for f_c has to be used to derive the phase-field equations, namely

$$f_c = \sum_i g_i(\vec{p})[B_i(T) - \mu A_i(T)], \qquad (3.49)$$

which is the form given in our preliminary account [32]. The mapping to single-phase solidification can be repeated: For the choice $h_i = p_i$, the result corresponds exactly to the isothermal variational model of Ref. [7]; as a result, Eqs. (3.40) and (3.47) hold again, with the same value of a_1 as before, but now with $a_2 = 1.175$.

The choice $h_i(\vec{p}) = p_i$ is quite advantageous for simulations, because the source term in Eq. (3.23) is less peaked inside the interface than for the fifth-order polynomial $g_i(\vec{p})$, which makes it possible to use a coarser discretization, resulting in a considerable gain in computational speed, as discussed in detail in Ref. [7].

G. One-sided model

We now address the one-sided case, for which the solute diffusivity in the solids is neglected compared to that of the liquid D. This is much more realistic for alloy solidification than the symmetric model considered up to now. We hence set

$$D(\vec{p}) = Dq(p_{\rm L}), \qquad (3.50)$$

with a function $q(p_{\rm L})$ that interpolates between 1 in the liquid and 0 in the solid.

This seemingly small change has important consequences. We already mentioned in Sec. II that a strictly vanishing solid diffusivity prevents solid–solid interfaces to move. For the solid–liquid interfaces, the introduction of a phase-dependent diffusivity breaks the symmetry of the impurity diffusion between solid and liquid. Furthermore, the variation of the diffusivity $D(\vec{p})$ through the diffuse solid–liquid interfaces needs to be considered in the asymptotic analysis, which becomes quite involved [8, 37]; we will only resume the most important points here.

It turns out that, in general, the effective free-boundary problem (FBP) obtained from the thin-interface analysis displays several terms that are not present in the original one and that scale with the interface thickness W. As explained in detail in Ref. [8], in analogy with the thermodynamics of diffuse interfaces these terms can be linked to "surface excesses", which are the integral through the interface of the excess of a quantity, where excess means the difference of its actual value at a point inside the diffuse interface region and its reference bulk value at the nearest side of the interface (the bulk values in the solid and the liquid might differ).

Let us consider the evolution equation for the chemical potential on the solid–liquid interfaces, Eq. (3.27), where the g_i were replaced by h_i as explained in the previous subsection. Three relevant surface excesses have been identified. The first is that of the "source function" $h_i(\vec{p})$: since it determines the equilibrium solute profile, an excess in this quantity confers a net impurity content to the interface (solute adsorption at the interface). The quantity of adsorbed solute increases with the area of the interface, which modifies the mass conservation condition, Eq. (2.5b), at moving curved interfaces (interface stretching). For the one-sided model, we have two more surface excesses: that of diffusivity $D(\vec{p})$, which leads to solute diffusion along the interface (surface diffusion) and thus also modifies the mass conservation condition; and that of the ratio $h_i(\vec{p})/D(\vec{p})$, which generates the well-known solute-trapping effect and shows up in the modified FBP in the form of a jump of the chemical potential through the interface [8].

For the symmetric model in which $D(\vec{p})$ is actually a constant, the choice of $h_i(\vec{p})$ odd with respect to the center of the interface ensures both the absence of interface stretching and of solute trapping. However, for the one-sided case, one has to eliminate surface diffusion too. The easiest way to do this is to also choose $D(\vec{p})$ odd. The simplest possible interpolation, $q(p_{\rm L}) = p_{\rm L}$, already satisfies this condition, and will be adopted in the following. The problem, however, is then that the surface excess of $h_i(\vec{p})/D(\vec{p})$ does not vanish, so that solute trapping is present.

With only two adjustable interpolation functions, one can generally not eliminate all three undesired surface excesses; more freedom is needed in the formulation of the model. One way to obtain this is to add a term counterbalancing one of the three effects, while choosing $h_i(\vec{p})$ and $D(\vec{p})$ to eliminate the other two. Here, we generalize to two-phase solidification one possible such term, originally introduced for single-phase solidification in Ref. [8]: We add to the solute current a new phenomenological contribution, an "antitrapping current" which drives the otherwise trapped solute into the liquid phase.

By analogy with Ref. [8], its form on each solid–liquid interface is easy to determine: It is directed parallel to the outward normal of the solid–liquid interface, and its magnitude is proportional to the interface thickness W and the intensity of the solute release which caused the trapping, $(A_{\rm L} - A_i)\partial h_i/\partial t$. How to interpolate this current between the two solid–liquid interfaces is less clear, since no asymptotic analysis or mapping to single-phase solidification is

available near a trijunction. We numerically tested various possibilities for interpolations, and chose the one that yielded the best convergence properties. It can be heuristically motivated as follows: The outward normal to each phase is given by $\hat{n}_i = -\vec{\nabla}p_i/|\vec{\nabla}p_i|$. Let us consider $\hat{n}_\alpha$. On the α–liquid interface, it is antiparallel to $\hat{n}_\mathrm{L}$, since $p_\alpha = 1 - p_\mathrm{L}$; in contrast, on the α–β interface it is antiparallel to $\hat{n}_\beta$, since $p_\alpha = 1 - p_\beta$. Upon growth, the α front advances along the direction of $\hat{n}_\alpha$ with a speed proportional to $\partial p_\alpha/\partial t$. The antitrapping current should always be directed towards the liquid, even if the solid formed is a "mixture" of both solid phases as happens in a trijunction; therefore, we choose to direct it along $\hat{n}_\mathrm{L}$ throughout the whole system. However, only the component of the growth speed directed toward the liquid should contribute to the magnitude of the antitrapping current; therefore, we multiply the source strength for each phase by the scalar product $-\hat{n}_\mathrm{L} \cdot \hat{n}_i$, which is equal to 1 on the solid–liquid interfaces, but smaller than 1 inside the trijunction.

The total concentration current thus reads

$$\vec{J} = -Dp_\mathrm{L}\vec{\nabla}\mu + 2aW\hat{n}_\mathrm{L} \sum_{i=\alpha,\beta} (A_\mathrm{L} - A_i)(-\hat{n}_\mathrm{L} \cdot \hat{n}_i)\frac{\partial p_i}{\partial t}, \tag{3.51}$$

where $2a$ is a prefactor to be adjusted, and we have taken $h_i = p_i$. Indeed, the particular form of the anti-trapping current given here is to be used *only* in conjunction with the simplest choices both for the diffusivity, as given in Eq. (3.50) with $q(p_\mathrm{L}) = p_\mathrm{L}$, and the source function, $h_i = p_i$; see Ref. [8] for further details.

With this new concentration current [Eq. (3.51)], we rederive Eq. (3.39):

$$\frac{\partial u}{\partial t} = D\vec{\nabla} \cdot \left(\frac{1 - \phi_i}{2}\vec{\nabla}u\right) + \frac{1}{2}\frac{\partial \phi_i}{\partial t} + aW\vec{\nabla} \cdot \left(\frac{\partial \phi_i}{\partial t}\frac{\vec{\nabla}\phi_i}{\left|\vec{\nabla}\phi_i\right|}\right). \tag{3.52}$$

We recover the quantitative phase-field model for one-sided solidification with a constant concentration gap given in Ref. [8]. Again, this has the advantage that we do not need to analyze the small-W behavior. From Ref. [8] we learn that the results of Eqs. (3.40) and (3.47) for d_i and β_i and the discussion thereafter still apply, and that $a = 1/(2\sqrt{2})$ is the value for which the term exactly counterbalances solute trapping. Interestingly, the values of a_1 and a_2 stay also the same as given before, for reasons explained in Ref. [8]. The fact that the only quantitative model for one-sided solidification available so far uses $h_i = p_i$ and that this choice enables one to recover the same numerical values for a_1 and a_2 as in the case of constant diffusivity is obviously another reason, on top of its lower numerical cost, to use $h_i = p_i$ instead of $h_i = g_i$.

H. Unequal surface tensions

As we have seen in Sec. III C 4, thanks to the particular form of our coupling f_c between phase and concentration fields, the surface tension, or equilibrium surface excess of the grand potential $f - \mu c$, reduces to the surface excess of the remaining two terms: f_grad and f_p. Since so far both f_grad and $f_p = f_\mathrm{TW}$ are symmetric with respect to the exchange of any two phases, the surface tensions of all interfaces are equal. In order to treat unequal surface tensions, this symmetry needs to be broken by modifying either of these two terms. In multi-phase-field models, different gradient energies are used for each interface [30]. In our approach, we want to maintain at least the condition of flatness, Eq. (3.9a), and it turns out to be easier to modify the potential part (see Appendix B for a detailed discussion).

We add a new term f_saddle to this potential part,

$$f_p = f_\mathrm{TW} + f_\mathrm{saddle}, \tag{3.53}$$

$$f_\mathrm{saddle} = \sum_i f_{\mathrm{saddle},i}. \tag{3.54}$$

f_saddle is due to change the height of the saddle points on each binary interface by a tunable, different amount, through the elementary functions $f_{\mathrm{saddle},i}$, which, in turn, should shift the saddle of f_TW separating phases j and k ($i \neq j, k$). Therefore, $f_{\mathrm{saddle},i}$ should vanish on interfaces other than the j–k one, and respect the valley character of all interfaces.

A function positive everywhere that vanishes on all sides automatically satisfies the latter two requirements, but obviously does not shift any saddle. However, it will be useful later on. The simplest such function is

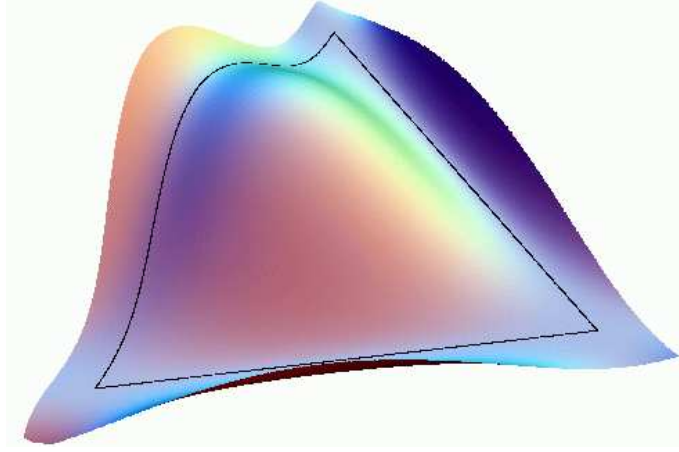$$f_\mathrm{obs} = p_1^2 p_2^2 p_3^2, \tag{3.55}$$

FIG. 6: Function used to lift the saddle between two phases and hence alter the surface tension. It is flat along the two unaltered interfaces. The position and strength of the hill in the middle are controlled by the parameter b in Eq. (3.56) (here, $b = 12$).

which corresponds to an elevation (obstacle) on the triple point and outside the Gibbs simplex. By dropping the p_i^2 factor we get a function which actually raises the saddle on the j–k interface and still vanishes and has valleys on the others, but which is not flat on the j–k interface in the direction perpendicular to it. We hence make the ansatz $f_{\text{saddle},i} = p_j^2 p_k^2 \tilde{f}_{\text{saddle},i}(\vec{p})$ and impose flatness at $p_i = 0$. The resulting condition for $\tilde{f}_{\text{saddle},i}$ reads $3(\partial \tilde{f}_{\text{saddle}}/\partial p_i)|_{p_\alpha + p_\beta + p_L = 1} = 2\tilde{f}_{\text{saddle}}/(p_j p_k)$ at $p_i = 0$, so that the simplest choice turns out to be $\tilde{f}_{\text{saddle},i} = 2p_j p_k + 3p_i$. This actually corresponds to a function that is small everywhere but in the neighborhood of the j–k saddle, where it is maximal. Therefore, its j–k side is flat but concave. To correct this concavity, we add to it the obstacle function f_{obs} given above,

$$f_{\text{saddle},i} = a_i p_j^2 p_k^2 (2p_j p_k + 3p_i + bp_i^2), \tag{3.56}$$

through the term in b. This composite function now has a valley that also runs along the j–k side as long as $b > 9/2$. The larger b, the closer the maximum of this function is to the triple point and the further to the j–k saddle. In Fig. 6, we show this function for $b = 12$.

On any purely binary interface $p_i = 0$, the whole function f_{saddle} reduces to $2a_i p^3 (1 - p)^3$, where p is any of the other phase fields. If we now put together the triple-well potential and the saddle functions, we find a free-energy density $f_p = f_{\text{TW}} + f_{\text{saddle}} = 2p^2 (1 - p)^2 [1 + a_i p(1 - p)]$ on such interfaces.

It is important to note that this modification does not affect the coupling between phase fields and concentration, and hence all the equilibrium compositions and the chemical potential remain the same as in the minimal model. In contrast, the surface tension is modified. Making use of the equipartition relation (i.e., the fact that $f_{\text{grad}} = f_{\text{TW}}$ for an equilibrium interface solution), we find the total surface excess per unit area of $f_{\text{grad}} + f_{\text{TW}}$ to be

$$\sigma_{jk} = 2\sqrt{2} W H \int_0^1 p(1 - p)\sqrt{1 + a_i p(1 - p)}\, dp, \ \ i \neq j, k. \tag{3.57}$$

Of course, for $a_i = 0$ the result reduces to Eq. (3.36). For $a_i \neq 0$, it is straightforward to evaluate this integral numerically and to tune the different surface tensions by using different a_i. However, the equilibrium profile of a j–k interface whose saddle has been shifted by a finite a_i is not any more the usual hyperbolic tangent solution of Eq. (3.30), but a kink-shaped profile that has to be calculated numerically. Since the equilibrium profile is the starting point for the entire asymptotic analysis, all calculations, and in particular the determination of the numerical constants a_1 and a_2 that appear in Eqs. (3.40) and (3.47), have to be repeated for this new profile, taking also into account the extra terms that are generated by f_{saddle} in the equations of motion. Similarly, the form of the antitrapping current needs to be adapted, using the methods of Ref. [8]. While this procedure is, in principle, straightforward, it is outside the scope of the present paper.

At this point, it is important to realize that the two solid–liquid surface tensions in many eutectic alloy systems are quite similar, and only the solid–solid surface tension is markedly different. This is, for instance, the case in CBr_4–C_2Cl_6. Therefore, using equal α–liquid and β–liquid surface tensions is usually a good approximation; only the solid–solid surface tension needs to be modified, and hence we have $a_\alpha = a_\beta = 0$, but $a_L \neq 0$. Then, we recover the

quantitative phase-field model on both solid–liquid interfaces; the solid–solid interface is not a problem, because it does not move (except close to the trijunction) in the one-sided model.

We should mention here that the computational effort to simulate the situation with unequal surface tensions ($a_k > 0$ for any k) is generally larger than for equal surface tensions ($a_k = 0 \; \forall k$). This is due to the fact that the free-energy landscape of a i–j interface whose saddle has been risen ($a_k > 0, \quad k \neq i, j$) is steeper than that of an unaltered interface, so that a smaller grid spacing Δx is necessary to discretize it in a convergent manner.

IV. NUMERICAL TESTS

A. Implementation

Our goal here is to show how the model derived in the preceding section is used in practice and to assess its validity and precision. We start by writing down the complete evolution equations for the one-sided, non-variational model with antitrapping current. They are essentially the same as Eqs. (3.22) and (3.23) of the minimal model, except that Eq. (3.22) now includes a contribution from f_{saddle}, $D(\vec{p}) = Dp_{\text{L}}$, the g_i have been replaced by $h_i = p_i$ in Eq. (3.23) but not in Eq. (3.22), and the total concentration current is now given by Eq. (3.51), which includes the antitrapping term. We make the equations dimensionless by scaling lengths by W ($\tilde{x} = x/W$, $\tilde{z} = z/W$, $\tilde{\vec{\nabla}} = W\vec{\nabla}$) and times by the $\bar{\tau} = (\tau_\alpha + \tau_\beta)/2$ used in the equation that sets $\tau(\vec{p})$, Eq. (3.46) ($\tilde{t} = t/\bar{\tau}$). The result reads

$$\tilde{\tau}(\vec{p})\frac{\partial p_i}{\partial \tilde{t}} = \tilde{\nabla}^2 p_i + \frac{2}{3}\left[-2p_i(1-p_i)(1-2p_i) + \sum_{j \neq i} p_j(1-p_j)(1-2p_j)\right]$$

$$+ 2\left\{a_i p_j p_k\left[(p_j + p_k)f_{a,i} - 2f_{b,i}\right] + \sum_{j \neq i} a_j p_i p_k\left[(p_i - 2p_k)f_{a,j} + f_{b,j}\right]\right\}$$

$$+ \tilde{\lambda}\sum_j \left.\frac{\partial g_j}{\partial p_i}\right|_{p_\alpha + p_\beta + p_{\text{L}} = 1}(\mu A_j - B_j) \quad \forall i, \tag{4.1}$$

$$\frac{\partial \mu}{\partial \tilde{t}} = \tilde{\vec{\nabla}} \cdot \left[\tilde{D}p_{\text{L}}\tilde{\vec{\nabla}}\mu\right] - \sum_i A_i \frac{\partial p_i}{\partial \tilde{t}}$$

$$+ 2a\sum_{i = \alpha, \beta}(A_i - A_{\text{L}})(-\hat{n}_{\text{L}} \cdot \hat{n}_i)\tilde{\vec{\nabla}} \cdot \left(\hat{n}_i \frac{\partial p_i}{\partial \tilde{t}}\right), \tag{4.2}$$

where $f_{a,k} \equiv p_i p_j + p_k(1 + bp_k/3)$, $f_{b,k} \equiv p_i p_j(1/2 + bp_k/3)$, and we recall that the $(\partial g_j/\partial p_i)|_{p_\alpha + p_\beta + p_{\text{L}} = 1}$ are given by Eqs. (3.24) and (3.25), that $\hat{n}_i = \vec{\nabla}p_i/|\vec{\nabla}p_i|$, and that we use $a = 1/(2\sqrt{2})$ to exactly counterbalance solute trapping.

Only dimensionless parameters remain in the equations, namely, the already dimensionless coefficients A_i, B_i, a_i, b, and $\tilde{\lambda}$, and the newly defined $\tilde{D} = D\bar{\tau}/W^2$ and $\tilde{\tau}(\vec{p}) = \tau(\vec{p})/\bar{\tau}$ [with its limiting values $\tilde{\tau}_\alpha = \tau_\alpha/\bar{\tau}$ and $\tilde{\tau}_\beta = \tau_\beta/\bar{\tau}$], where $\tau(\vec{p})$ is given by Eq. (3.46). The coefficients $A_i(T)$ and $B_i(T)$ are just constants for isothermal solidification, but depend on space and time (through the temperature) for directional solidification. Their explicit expression, given when choosing the phase diagram in next subsection, will contain the rescaled pulling speed $\tilde{v}_p = v_p\bar{\tau}/W$ and thermal lengths $\tilde{l}_{\text{T}}^i = l_{\text{T}}^i/W$.

We numerically integrate Eqs. (4.1) for p_α and p_β only (the equation for p_{L} is redundant) as well as Eq. (4.2); p_{L} is eliminated everywhere through $p_{\text{L}} = 1 - p_\alpha - p_\beta$. We use a simple Euler, forward-time, centered-space finite-difference scheme with a grid spacing $\Delta\tilde{x}$ and a time step $\Delta\tilde{t}$ slightly below the stability limits of both the discretized diffusion and the phase-field equations, the lowest of which reads $\Delta\tilde{t} = (1/4)(\Delta x/W)^2 \min\{1/\tilde{D}, \tilde{\tau}_\alpha, \tilde{\tau}_\beta\}$. We use standard second-order accurate finite differences, except for the Laplacians, which are discretized by a nine-point formula involving nearest and next nearest neighbors to reduce lattice anisotropy. We use $\Delta\tilde{x} = 0.8$ unless otherwise stated, which is the largest value for which most results are numerically converged. Exceptionally, some parameter sets require $\Delta\tilde{x} = 0.4$.

We simulate two-dimensional directional (or, in one case, isothermal) solidification in a rectangular simulation box of total size $n_x \times n_z$, where n_x and n_z are the number of grid points in the direction perpendicular and parallel to the thermal gradient, respectively. We consider perfectly periodic lamellar arrays. A minimal representation of this geometry consists of a simulation box with no-flux boundary conditions in both the x and z directions and two adjacent half lamellae, one of each phase, with their centers on the box boundaries and the trijunction in the middle. Typically, we start with completely flat interfaces, and the phase fields are initialized as step functions, located at
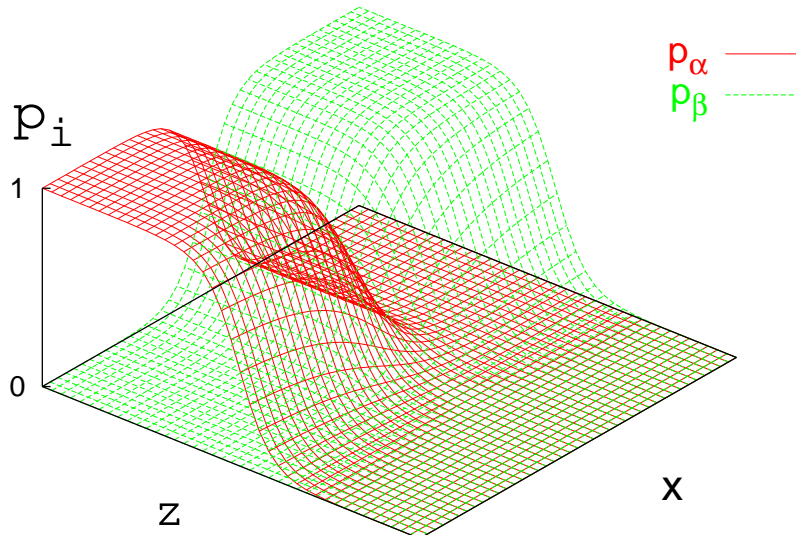
FIG. 7: Illustrative surface plot of the two phase fields p_α and p_β, for two half lamellae as described in the text. 40×40 grid points shown; the system is actually larger in the z direction.

some initial guess for the interface position. These step functions then quickly relax to the smooth solutions for the phase fields, while the interfaces begin to curve and drift to adjust their average undercooling. Alternatively, the outcome of a previous simulation may also be taken as initial condition. An example for the resulting configuration of the phase fields is shown in Fig. 7. It can be clearly seen that the fields smoothly approach their bulk equilibrium values outside the interfaces, and that, on each i–liquid interface (at $x =$const. sufficiently far from the solid–solid interface), the other solid phase, $j \neq i$, is absent ($p_j = 0$) through the entire interface (as z varies).

In order to reduce the computational effort, we take advantage of two circumstances. First, as can be seen in Fig. 7, most grid points correspond to bulk phases, so that the evolution equations can be replaced there by simpler versions, which leads to an enormous saving in the total number of operations per time step. Furthermore, most of the remaining grid points correspond to purely binary interfaces, so that all the terms in the third, vanishing phase field can be dropped. Only in the small area near a trijunction do the full equations need to be integrated. According to the conditions Eqs. (3.9), wherever a phase field takes a locally *constant* value of zero (purely binary interface or bulk phase) or unity (bulk phase), it will remain constant, so that it does not need to be updated, and its whole evolution equation can be dropped. In practice, we first compute the Laplacian of each phase field everywhere, and then proceed with further calculations for a phase field p_i only if the modulus of its Laplacian exceeds a certain (small) threshold. Similarly, the source and antitrapping terms in the evolution equation for the chemical potential in Eq. (4.2) are evaluated for the locally varying phase field(s) only. In particular, this means that they can be dropped for bulk phases. Therefore, in the bulk only the simple diffusion equation needs to be solved; in the one-sided model, no field needs to be updated in the solid, be it bulk or $\alpha - \beta$ interface.

Second, since the diffusion and thermal lengths are much larger than the lamellar spacing, the number n_z of grid points required in the direction of the thermal gradient is typically much larger than n_x. A simple analytical calculation (see for example Ref. [36]) shows that the lateral gradients of the diffusion field decay with the distance to the growth front over a length of the order of the interfacial pattern ($\sim n_x$), whereas in the direction of the pulling the solutal boundary layer decays only on the scale of the diffusion length. Therefore, the spatial resolution can be decreased with the distance to the growth front beyond a scale comparable to n_x. This can be achieved by multi-scale algorithms. We have adapted the random walker algorithm of Ref. [41] to eutectic solidification; however, a disadvantage of this method is its numerical noise. For our relatively simple geometry, it is straightforward to implement a finite-difference scheme that uses coarser and coarser grids away from the interface. We used a hierarchy of in total three grids of increasing length in the z direction as sketched in Fig. 8. The solutions on the different grids are connected by simple linear interpolation. At the end of the coarsest grid, lateral concentration gradients are negligibly small; therefore, we solve the diffusion equation in one dimension beyond this point and connect the solution to the coarsest grid. We carefully checked that the dependence of the solution on the position of the interpolation boundaries is negligible.
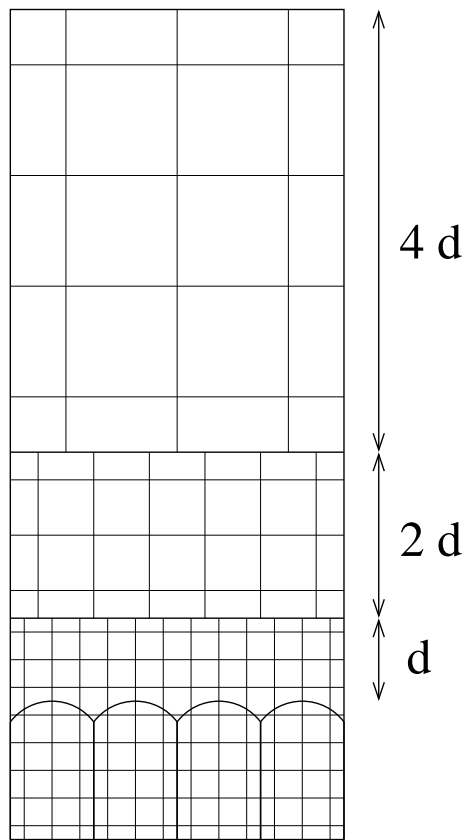
FIG. 8: Configuration of the multi-grid scheme. In front of the solids that grow upward, a fixed number n_f of rows is treated on the fine grid with spacing Δx, which corresponds to a distance $d = n_f \Delta x$. Two coarser grids of spacing $2\Delta x$ and $4\Delta x$ have again n_f rows each, which corresponds to distances $2d$ and $4d$, respectively. Beyond the coarsest grids, the solution is one-dimensional.

Finally, we also follow the solidifying front by advancing the simulation box whenever the isotherms have advanced by once the coarsest grid spacing. Since, far enough in the solid, the diffusivity vanishes and no evolution takes place, the coldest part of the solid can be removed without altering the simulation; new points are added on the liquid side. The boundaries between grids are also adjusted, and new initial values on the border of the finer grids are obtained by interpolation from the coarser grids.

B. Choice of parameters

The parameters that characterize a given physical situation can be grouped into different classes. First, there are the characteristics of the phase diagram and some materials parameters that depend only on the alloy system. Second, there are the control parameters accessible to the experimentalist, namely the sample composition and either the undercooling for isothermal solidification, or the pulling speed v_p and the temperature gradient G for directional solidification. Finally, there is the lamellar spacing, which cannot be directly controlled in experiments, but can be fixed in the simulations by choosing appropriate initial and boundary conditions.

For coupled eutectic growth at low solidification speeds, we can make several simplifying assumptions and approximations in order to keep the number of relevant parameters to a minimum. Since the average temperature of the solidification front is very close to T_E, we can (i) use a phase diagram linearized around the eutectic point, as specified in Eq. (2.2) of the FBP. This can be implemented by setting the parameters A_i and B_i to

$$A_{\mathrm{L}} = 0, \quad A_i = c_i \mp \frac{(k_i - 1)(T - T_{\mathrm{E}})}{m_i \Delta C} = c_i \mp (k_i - 1)\frac{\tilde{z} - \tilde{v_p}\tilde{t}}{\tilde{l}_{\mathrm{T}}^i}, \tag{4.3}$$

$$B_{\mathrm{L}} = 0, \quad B_i = \mp\frac{A_i(T - T_{\mathrm{E}})}{m_i \Delta C} = \mp A_i\frac{\tilde{z} - \tilde{v_p}\tilde{t}}{\tilde{l}_{\mathrm{T}}^i}, \tag{4.4}$$

TABLE I: Materials parameters of the transparent alloy CBr$_4$–C$_2$Cl$_6$, as measured in Ref. [33], and the values used for the present study (see text). The d_i listed under Ref. [33] were obtained using the basic definitions of Eq. (2.9) together with the thermophysical data from that reference. The value of C_E used corresponds to $r_c \equiv 2.5$.

Quantity	Symbol	Ref. [33]	Value used
Liquidus slope of α	m_α	$-(81 \pm 5)$ K/mol	-82 K/mol
Liquidus slope of β	m_β	(165 ± 5) K/mol	164 K/mol
Composition of α at T_E	C_α	(8.8 ± 0.4) mol%	8.8 mol%
Composition of β at T_E	C_β	(18.5 ± 0.9) mol%	18.5 mol%
Eutectic composition	C_E	(11.6 ± 0.6) mol%	11.571 mol%
Capillary length of α	d_α	(9.5 ± 2.0) nm	9.29 nm
Capillary length of β	d_β	(3.5 ± 1.0) nm	3.71 nm
Contact angle of α	θ_α	$(70 \pm 10)°$	$30°$–$66°$
Contact angle of β	θ_β	$(67 \pm 10)°$	$30°$–$66°$
Partition coefficient of α	k_α	0.75	1.0
Partition coefficient of β	k_β	1.5	1.0
Impurity diffusivity	D	$(0.5 \pm 0.1) \times 10^{-9}$ m^2/s	0.5×10^{-9} m^2/s

where the second equalities are obtained using Eq. (2.1) for the temperature and the definitions of the thermal lengths, Eq. (2.8). Furthermore, we can (ii) neglect the relative variation of the concentration gaps with respect to their values at T_E. This is equivalent to set $k_i = 1$ (parallel liquidus and solidus lines) in Eq. (2.5b) [42]. The advantage here is that two parameters (the k_i) are eliminated and that the A_i become independent of temperature. Finally, at low solidification speeds we can also (iii) neglect the kinetic undercooling of the growth front, i.e., we adopt $\beta_\alpha = \beta_\beta = 0$, which is also the most reasonable choice with the information available, since these coefficients are unknown. All of these approximations were also made in the classic Jackson-Hunt analysis [36].

Furthermore, we use equal surface tensions for both solid–liquid interfaces ($\sigma_{\alpha L} = \sigma_{\beta L}$), which implies equal contact angles $\theta_\alpha = \theta_\beta \equiv \theta$. This is a reasonable assumption with the available data for CBr$_4$–C$_2$Cl$_6$ $\theta_\alpha = 70° \pm 10°$ and $\theta_\beta = 67° \pm 10°$ [33]. In our test calculations below, we use values of the computational parameters for which angles ranging from $\theta = 30°$ (all surface tensions equal) to $66°$ (case of CBr$_4$–C$_2$Cl$_6$) are expected.

With approximations (i) and (ii) above, the phase diagram can be characterized by the two ratios

$$r_m = m_\beta/m_\alpha, \tag{4.5}$$
$$r_c = |c_\beta/c_\alpha|. \tag{4.6}$$

Note that we have $c_\beta - c_\alpha = 1$ due to the normalization, and hence it follows that $c_\beta = r_c/(r_c+1)$ and $c_\alpha = -1/(r_c+1)$. The measured properties for CBr$_4$–C$_2$Cl$_6$ are listed in Table I. According to the constraint of Eq. (3.45), for equal surface tensions we should have $d_\alpha/d_\beta = r_c$. From Table I, we find $d_\alpha/d_\beta = 2.7 \pm 0.5$, while $r_c = 2.5 \pm 0.5$. Thus, the constraint is respected to within the accuracy of the measured data. For our simulations, we have to choose a set of values that exactly satisfies the constraint and is compatible with the experimental error bars. We use the concentrations to fix $r_c = d_\alpha/d_\beta = c_\beta/c_\alpha = 2.5$, and take as a reference length the average

$$\bar{d} = (d_\alpha + d_\beta)/2 \tag{4.7}$$

of the measured capillary lengths, $\bar{d} = 6.5$nm. The capillary lengths obtained using this value of $\bar{d}$ together with $r_c = 2.5$ and the constraint are listed on the last column of Table I. Similarly, we choose $r_m = 2$ and fix a corresponding pair of values for the liquidus slopes within the error bars. Finally, we adopt the mean measured value of the solute diffusivity, $D = 0.5 \times 10^{-9}$ m^2/s. The measured and used values of the parameters are summarized in Table I.

The control parameters which can be varied in an experiment enter our simulations as follows. The global sample composition is fixed by imposing the appropriate value for the chemical potential $\mu(z \to \infty) = c_\infty$ (recall that $A_L = 0$) as a boundary condition on the liquid side of the simulation box. For isothermal solidification, the undercooling enters through Eqs. (4.3) and (4.4) in dimensionless form, $\Delta_i = (T_E - T)/(m_i \Delta C)$. For directional solidification, the pulling speed v_p and the thermal gradient G enter through the same equations via the diffusion and thermal lengths $l_D = D/v_p$ and $l_T^i = m_i \Delta C/G$. Note that $l_T^\beta/l_T^\alpha = r_m$, so that $l_T^\alpha = [2/(1+r_m)]\bar{l}_T$ and $l_T^\beta = [2r_m/(1+r_m)]\bar{l}_T$, where we recall that $\bar{l}_T = (l_T^\alpha + l_T^\beta)/2$ is the average thermal length. Finally, the lamellar spacing λ (not to be confused with the coupling constant $\tilde{\lambda}$) is fixed by the lateral size of the simulation box.

To summarize, the physical conditions to simulate are completely specified by the two asymmetry parameters r_c and r_m and four lengths, namely, $\bar{d}$, $\bar{l}_T$, l_D and λ. From these four length scales, three dimensionless parameters can

TABLE II: Simulation parameters used in the runs for the symmetric model alloy. Physical parameters are $l_D/\bar{d} = 51200$, $\bar{l}_T/l_D = 4$, $\lambda = \lambda_{\mathrm{JH}}$, and the sample is at eutectic composition. Space and time units are W and $\bar{\tau}$, respectively.

λ/W	$\tilde{D}$	$\tilde{\lambda}$	$\tilde{v}_p$	$\bar{l}_T/W$	$\Delta t/\bar{\tau}$
32	10.633	36.197	0.0079729	5334.5	0.012038
64	5.3164	18.098	0.0019932	10669	0.024077
96	3.5442	12.066	0.00088588	16003	0.036115
128	2.6582	9.0491	0.00049831	21338	0.048153

be constructed. We choose $l_D/\bar{d}$, $\lambda/\lambda_{\mathrm{JH}}$, and $\bar{l}_T/l_D$. The second choice is motivated by the fact that the Jackson-Hunt minimum undercooling spacing is a reference length for eutectic pattern formation. Dividing both sides of Eq. (2.17) by $\bar{d}$ yields $\lambda_{\mathrm{JH}}/\bar{d} \propto \sqrt{l_D/\bar{d}}$, where the proportionality constant depends only on the sample composition (through the volume fraction η) and on r_c (through the ratios $d_i/\bar{d}$). Therefore, specifying $\lambda/\lambda_{\mathrm{JH}}$ and $l_D/\bar{d}$ fixes implicitly $\lambda/\bar{d}$.

All physical conditions fixed, we now choose the only truly free computational parameter, the interface thickness W. The relevant scale of the pattern is of course the lamellar spacing λ, and therefore the resolution of the phase-field simulations is given by the ratio λ/W. Let us first outline the procedure to determine the parameters when the spacing is given in physical units (meters). Then, λ/W directly fixes W in meters. Next, the coupling constant $\tilde{\lambda}$ is determined from Eqs. (3.40) for the capillary lengths in terms of phase-field parameters (recall that $A_{\mathrm{L}} = 0$),

$$\tilde{\lambda} = \frac{W}{\bar{d}} \frac{a_1}{2} \left(\frac{1}{|A_\alpha|} + \frac{1}{|A_\beta|} \right). \tag{4.8}$$

Finally, the relaxation times τ_i (in seconds) are obtained (for arbitrary kinetics) using Eq. (3.47),

$$\tau_i = \tilde{\lambda} |A_i| W \left(\frac{\beta_i}{a_1} + a_2 \frac{|A_i|W}{D} \right), \tag{4.9}$$

which yields $\bar{\tau} = (\tau_\alpha + \tau_\beta)/2$ and the $\tilde{\tau}_i = \tau_i/\bar{\tau}$. The diffusion coefficient $\tilde{D}$, pulling speed $\tilde{v}_p$, and thermal lengths $\tilde{l}_{\mathrm{T}}^i$ needed in Eqs. (4.1) and (4.2) are then obtained by scaling the corresponding dimensional quantities by W and $\bar{\tau}$. For isothermal solidification, the dimensionless undercooling Δ_i is directly obtained from the actual temperature T and the alloy properties T_{E}, m_i and ΔC.

An alternative way to obtain the simulation parameters is to start directly from the dimensionless ratios. Indeed, specifying λ/W for fixed $\lambda/\bar{d}$ fixes directly $W/\bar{d}$ and hence $\tilde{\lambda}$ from Eq. (4.8). For $\beta_\alpha = \beta_\beta = 0$, Eq. (4.9) yields $\tilde{\tau}_\beta/\tilde{\tau}_\alpha = (|A_\beta|/|A_\alpha|)^2$. For the case $k_i = 1$ considered here, $A_i = c_i$, and hence $|A_\beta|/|A_\alpha| = r_c$, and we obtain directly $\tilde{\tau}_\alpha = 2/(1 + r_c^2)$ and $\tilde{\tau}_\beta = 2r_c^2/(1 + r_c^2)$. With these values fixed, Eq. (4.9) with the c_i given after Eqs. (4.5) yields the scaled diffusivity,

$$\tilde{D} = (1/2)a_2\tilde{\lambda}(1 + r_c^2)/(1 + r_c)^2. \tag{4.10}$$

Since $W/\bar{d}$ and $l_D/\bar{d}$ are both known, the scaled pulling speed can then be inferred from $l_D/W = \tilde{D}/\tilde{v}_p$; finally, the scaled thermal lengths are obtained via the ratio $\bar{l}_T/l_D$ for directional solidification, or the dimensionless undercooling Δ_i is directly plugged into the A_i's and B_i's for isothermal solidification.

To illustrate the above procedure, we show in Tables II and III the computational parameters for different values of the interface thickness for two series of test simulations that will be discussed in detail below. Both sets of simulations are carried out at the eutectic composition and for a spacing $\lambda = \lambda_{\mathrm{JH}}$. The first is for a model alloy with a symmetric phase diagram, $r_m = r_c = 1$. For such an alloy at the eutectic composition, all equations are completely symmetric with respect to the interchange of the two solid phases. In this case, we use $\bar{l}_T/l_D = 4$ and $l_D/\bar{d} = 51200$. The second set of simulations is for the phase diagram of CBr$_4$–C$_2$Cl$_6$, $r_c = 2.5$ and $r_m = 2$, and we use $l_D/\bar{d} = 41796$ and $\bar{l}_T/l_D = 4$, which corresponds to a pulling speed of $v_p \approx 1.8$ μm/s and a temperature gradient of $G \approx 110K$/cm, both fairly typical experimental values.

Finally, the a_i are dimensionless parameters that control the ratio of surface tensions through the relative heights of the free-energy barriers between bulk phases. They hence provide a handle on the contact angles. The choice of the a_i is independent of all the other parameters. For equal solid–liquid surface tensions, we recall that $a_\alpha = a_\beta = 0$; a_{L} will then be varied in the next subsection to tune the ratio of solid–liquid to solid–solid surface tensions, and thus change the solid–liquid contact angle θ. A change from $a_{\mathrm{L}} = 0$ to $a_{\mathrm{L}} = 12$ is necessary to span contact angles from $0°$ to $66°$ as desired. On the other hand, b needs to be tuned to ensure the convexity of the free-energy landscape; we test values ranging from $b = 3$ to $b = 12$.

TABLE III: Simulation parameters used in the runs for CBr$_4$–C$_2$Cl$_6$. Physical parameters are $l_D/\bar{d} = 41796$, $\bar{l}_T/l_D = 4$, $\lambda = \lambda_{\mathrm{JH}}$, and the sample is at eutectic composition. Space and time units are W and $\bar{\tau}$, respectively.

λ/W	$\tilde{D}$	$\tilde{\lambda}$	$\tilde{v}_p$	l_T^{α}/W	l_T^{β}/W	$\Delta t/\bar{\tau}$
32	14.852	42.713	0.013141	3013.7	6027.4	0.0086186
64	7.4258	21.357	0.0032854	6027.4	12055	0.017237
96	4.9505	14.238	0.0014602	9041.1	18082	0.025856
128	3.7129	10.678	0.00082134	12055	24110	0.034474

C. Isothermal solidification and contact angles

We begin our simulations by testing whether our model reproduces the correct contact angles at the trijunction point. For that purpose, we need to extract first the interface shapes, then the trijunction position, and finally the angles between interfaces from the simulations. We proceed as follows.

The difference $p_j - p_i$ is computed everywhere, for every pair of phases $i \neq j$. Wherever one of these combinations changes sign, we interpolate the position of a i–j interface point from the two adjacent values of $p_j - p_i$; we also interpolate the value of the third phase p_k at that point. If $p_k < 1/3$, the point lies on a "true" i–j interface; otherwise, it is located inside the third bulk phase on the "prolongation" of the interface beyond the trijunction point. In most cases, the latter points are not plotted, and the i–j interface terminates at the trijunction; however, as we will see below, it is sometimes useful to plot the prolongation as well, because it can yield information about the internal structure of the trijunction. The average undercooling of each interface is obtained from the z position of all of its points. In order to avoid sharp cutoffs and discretization errors at trijunctions, the contribution of each point on the $p_i = p_j$ isocontour to the undercooling is weighted by $1 - p_k$, rather than simply counting points on the "true" interface and discarding points on the prolongation.

When all three interfaces enter and leave a particular elementary grid square exactly once, their entrance and exit positions computed by the method described above define one straight segment for each interface. If all three segments intersect with each of the other two, a triple point is considered to be detected at the average position of the three intersections, provided that this lies within the grid square. While this procedure yields an excellent subgrid resolution for the position of the trijunction points, the determination of the angles from the slopes of the segments is subject to large grid effects (that is, the values obtained are found to depend on the position of the trijunction with respect to the grid points). Therefore, we use a more precise procedure: Around a detected trijunction point, a few interface points on both side of the trijunction are first obtained with high precision using nonlinear interpolations. Then, two such points on each side of the trijunction are used together with a nonlinear interpolation to obtain the angles at the trijunction position. With this procedure, the uncertainty on the angles due to grid effects is reduced to about $0.1°$.

Before engaging in directional solidification, we test both the model and the above procedures by simulations of isothermal solidification, in which the temperature is set to a constant value below the eutectic temperature; in the free-boundary problem, the terms $(z_{\mathrm{int}} - v_p t)/l_T^i$ are then replaced by constants $-\Delta_i$ where $\Delta_i = (T_{\mathrm{E}} - T)/(m_i \Delta C)$ is the dimensionless undercooling of phase i ($i = \alpha, \beta$). Since the interface temperature is fixed, the quantity to be selected is now the interface velocity. This velocity is negative for low undercooling (the lamellae melt), positive for high undercooling, and exactly zero for a critical undercooling that depends on the lamellar spacing through the curvature of the solid–liquid interfaces. For the symmetric model alloy at the eutectic composition, an exact solution for this critical steady state is known: Since the composition in the liquid and the temperature are uniform and the velocity is zero, the interface curvature is constant [see, for instance, Eq. (2.2)], so that the two solid–liquid interfaces form circular arcs that intersect at the trijunction point. For a given contact angle and lamellar spacing, the critical undercooling is

$$\Delta_c = 4 \sin \theta \frac{\bar{d}}{\lambda}. \tag{4.11}$$

We conducted series of simulations with different undercoolings and extracted the velocity of the solid–liquid interface once it had reached a steady state; the critical undercooling was obtained by seeking the zero crossing of the velocity. The grid spacing was fixed to $\Delta x = 0.4$ to better resolve the neighborhood of the critical undercooling (small velocities), and the parameters of the first line in Table II (except $\tilde{v}_p$ and $\tilde{l}_T$) were used. We tested five different values of a_{L} for which equilibrium angles from $\theta = 30°$ to $\theta = 66°$ are expected from Young's law, with a constant $b = 12$. The predicted angle was then plugged into Eq. (4.11) to obtain the theoretical value of the critical undercooling. The latter is then compared to its measured value, as summarized in Table IV. We find excellent agreement between

TABLE IV: Critical undercooling for stationary lamellar states for various values of a_L (and hence of the contact angle θ); $b = 12$ in all cases, and the other parameters are given in the first line of Table II.

a_L	θ expected	Δ_c (simulation)	$\Delta_c(\theta)$ (theory)	error
0	30°	0.001624	0.001628	0.25%
3	39°	0.002047	0.002055	0.39%
6	48°	0.002390	0.002408	0.75%
9	56°	0.002686	0.002713	1.00%
12	66°	0.002946	0.002987	1.37%
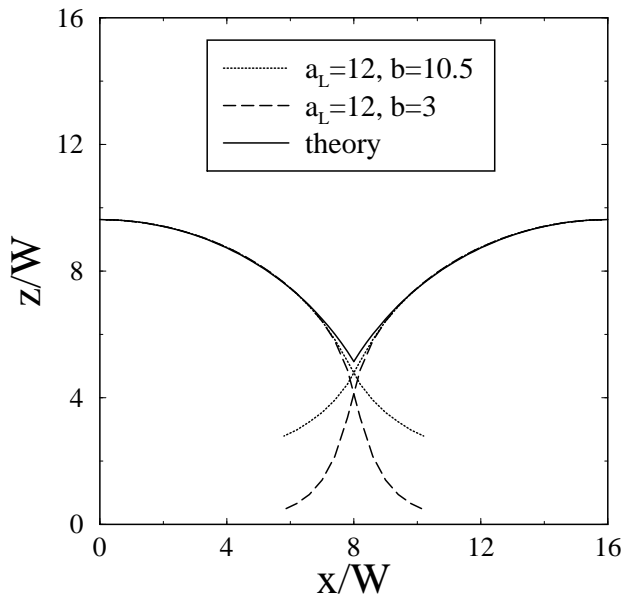
FIG. 9: Lamellar states, simulated with a constant temperature that yields almost zero growth speed, and comparison to the analytical critical stationary solution that consists of circular arcs. Two different values of b are used together with $a_L = 12$ (predicted angle $\theta \approx 66°$). Since, at constant temperature, the origin of the z axis is arbitrary, the solutions have been shifted in order for lamella tips to coincide. The curves shown are the isocontours $p_\alpha = p_L$ and $p_\beta = p_L$, to be compared with the theoretical circle arcs with the predicted contact angle θ (solid curve). The isocontour $p_\alpha = p_\beta$, exactly vertical and located at $x/W = 8$, has been omitted for clarity.

simulations and theory; the error in the undercooling increases with a_L (and hence with the contact angle), but remains of the order of 1% even for $a_L = 12$, which corresponds to $\theta = 66°$. In particular, this implies that Young's law is satisfied.

However, if we measure the contact angles *directly* using the numerical procedure outlined above, we find a consistent result only for $a_L = 0$, that is, the measured contact angles are *always* very close to 30°; for $a_L \neq 0$, we find angles that differ widely from the expected values. Furthermore, whereas the detected critical undercooling is almost independent of the parameter b, the measured angles for $a_L = 12$ vary by 20° when b is varied between 3 and 12.

The reason for this behavior becomes apparent in Fig. 9. We show the analytical solution, which consists of two circular arcs with contact angles $\theta = 66°$, as well as the interfaces extracted from the simulations for two different values of b. Whereas the agreement between the two simulations and the theory is excellent far from the trijunction, the three shapes start to become different at a distance of about W from the trijunction. The lines $p_i = p_j$ exhibit curvatures which differ from the curvature of the circular arcs of the analytical solution, and which depend on the value of b; the position of the trijunction point also depends on b. This behavior is due to the changes in the potential energy landscape induced by the variations of b, which affects the internal structure of the trijunction region. Note, however, that the radius of curvature of the solid–liquid interfaces far from the trijunction does not change. This implies that the critical undercooling remains the same, and hence that Young's condition and the contact angles extrapolated from the interfaces to the trijunction are correctly implemented in all cases.

The lesson from all this is that the local procedure outlined above does in general not yield the "macroscopic" angles, but values that are influenced by the internal structure of the trijunction region. A different possibility to

obtain the "macroscopic" angles would be to construct the intersection of the two solid–liquid interfaces, extrapolated from their shape outside the trijunction. However, this procedure is prone to large errors out of equilibrium, since the curvature varies along the interfaces. As a consequence, contact angles are very hard to measure in out-of-equilibrium situations when $\theta \neq 30°$. When $\theta = 30°$, the "local" procedure works properly. The particularity of this value is, of course, the symmetry between all three phases, which entails that the prolongation of the interface inside the third phase runs exactly in the middle between the two other interfaces and is not "deflected" from the direction in which it enters the trijunction. In contrast, for $a_L \neq 0$, the local shape and curvature of this isoline depend on the internal structure of the trijunction, which explains the errors made in the "local" measurement of the angles.

Since we are interested in precise information on the angles, we restrict all the following simulations to the case of equal surface tensions, where reasonably accurate measurements of the angles can be carried out. An additional advantage of this choice is that it avoids the reduced grid spacing needed to resolve the steeper interfaces associated to a higher surface tension. For $a_L = 12$ (which corresponds to the actual value of θ in CBr$_4$–C$_2$Cl$_6$), Δx needs to be divided by a factor of 2 ($\Delta x = 0.4$) with respect to $a_L = 0$, which implies using a 4 times larger system size (in terms of grid points) running for 4 times more time steps (recall that $\Delta t \propto \Delta x^2$), which hence takes 16 times more CPU time. Having tested the equilibrium angles, in the remaining subsections we focus on out-of-equilibrium simulations of directional solidification.

D. Steady state lamellae

The convergence of our model to the thin-interface predictions is tested by performing series of simulations for fixed physical parameters and decreasing interface width. For each simulation, the interface profiles and interface undercooling are monitored to check when the steady state is reached. For comparison, the same series of runs is also performed without the antitrapping current, and for an earlier version of our model presented in Ref. [26] that uses different interpolation functions g_i. Since those functions are not antisymmetric with respect to the point $p_i = p_j = 1/2$ on i–j interfaces [i.e., they do not satisfy Eq. (3.15)], this model exhibits several thin-interface corrections [8, 37].

The parameters used for the simulations of the model alloy with symmetric phase diagram are listed in Table II. Simulation times on a 2.4 GHz Intel Xeon processor range from half an hour for the lowest resolution ($\lambda/W = 32$) to three days for the highest ($\lambda/W = 128$). The results for the interface profile are shown in Fig. 10, together with results of boundary integral calculations performed with the code of Ref. [17]. Whereas for the present model all curves for $\lambda/W \geq 64$ superimpose perfectly, for the other models large errors appear. It can be seen that they are smaller for the model that only lacks the antitrapping current; however, a decisive progress is made only when all thin-interface corrections are eliminated. Even so, a small difference with the boundary integral prediction remains in the $W/\lambda \to 0$ limit. However, a close examination reveals that the two solutions are simply shifted with respect to each other, with is due either to a residual interface kinetics in the phase-field model or to the approximations of the boundary integral method. The relative error in the average undercooling is about 0.3 %. Since the advantage of the complete model over the other formulations is obvious, it has been used exclusively for all the remaining simulations.

We also examine the contact angles at the trijunction point for the same series of runs with the complete model. We find small deviations from the expected equilibrium value of 30°. In Fig. 11, we plot the difference, $30° - \theta$, as a function of W/λ. It can be seen that it extrapolates to zero in the $W/\lambda \to 0$ limit. This indicates that there is a finite-interface-thickness correction to the *non-equilibrium* contact angles that vanishes in the sharp-interface limit. Since the difference is smaller than 2° for $\lambda/W \geq 64$, this effect is invisible in the profiles and does not appreciably influence the results for the undercooling. In particular, it cannot be responsible for the 0.1% undercooling mismatch described above, since the latter does not extrapolate to zero in the $W/\lambda \to 0$ limit.

We now consider the dependence of the average undercooling of the front ΔT on the lamellar spacing λ, which is known as the Jackson–Hunt curve, Eq. (2.15). We perform a series of runs for the same materials and computational parameters as above, but with varying box size (and hence lamellar spacing). For the resolution, we take $\lambda_{JH}/W = 32$ and 64, since, on the basis of Fig. 10(a), we expect results to be converged for $\lambda_{JH}/W \geq 64$. The curves thus obtained are plotted in Fig. 12, for the first ($\lambda_{JH}/W = 32$, squares) and second ($\lambda_{JH}/W = 64$, circles) set of parameters of Table II. The undercooling ΔT, scaled by $m\Delta C$, can be directly obtained through $\Delta T/(m\Delta C) = \langle z_{int} \rangle/l_T$ (note that for the symmetric model alloy, the two liquidus slopes and hence also the two thermal lengths are equal, $m_\alpha = m\beta = m$ and $l_T^\alpha = l_T^\beta = l_T$), where $\langle z_{int} \rangle$ is the z position of the solid-liquid interface, averaged over the lateral coordinate x. The line shows the best fit of the higher resolution data to the Jackson-Hunt law, Eq. (2.15), with ΔT_{JH} and λ_{JH} as free parameters. The fit yields $\lambda_{JH}/l_D = 0.02468$ and $\Delta T_{JH}/(m\Delta C) = 0.003023$, whereas the theoretical values calculated from Eqs. (2.17) and (2.16) are 0.02403 and 0.003251, respectively; this corresponds to relative differences of 2.7 % and 7.0 %, respectively. This good agreement is especially noteworthy because in phase-field models which exhibit thin-interface corrections the difference between simulated and calculated minimum undercooling spacings is usually much larger [18, 25, 27]. Note that the Jackson–Hunt prediction for the minimal undercooling and its corresponding
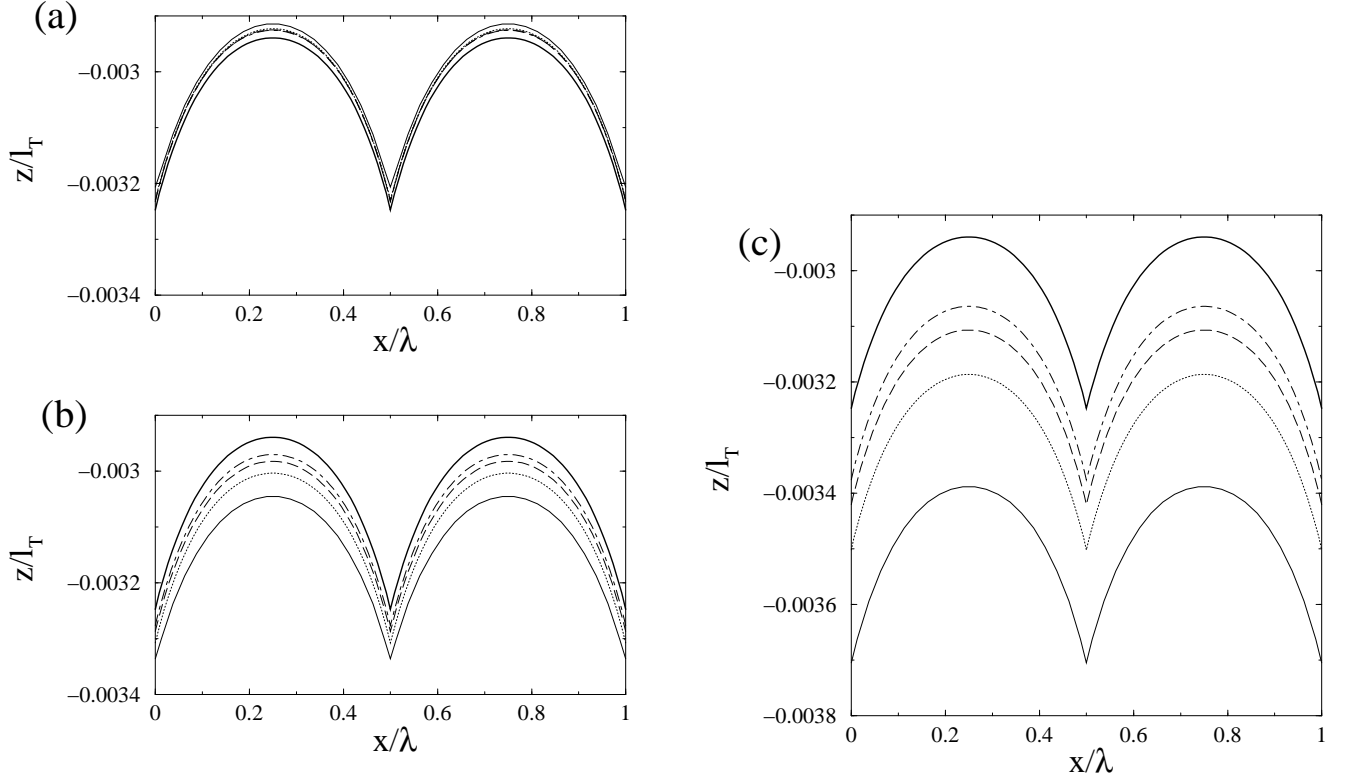
FIG. 10: Convergence test for lamellar shapes in the symmetric model alloy at the eutectic composition. The solid–liquid interfaces are plotted for (a) the complete model, (b) without the antitrapping current, and (c) a model with several thin-interface corrections taken from Ref. [26]. The parameters for all runs are given in Table II. Thin solid lines: $\lambda/W = 32$, dotted lines: $\lambda/W = 64$, dashed lines: $\lambda/W = 96$, dash-dotted lines: $\lambda/W = 128$; thick solid line: result of the boundary integral code of Ref. [17].
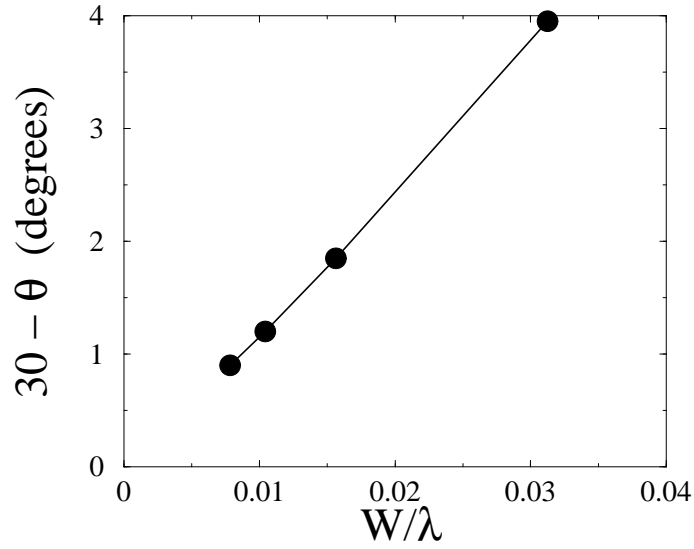
FIG. 11: Difference between the contact angle and the equilibrium value $30°$ as a function of W/λ for the same series of runs as Fig. 10(a).
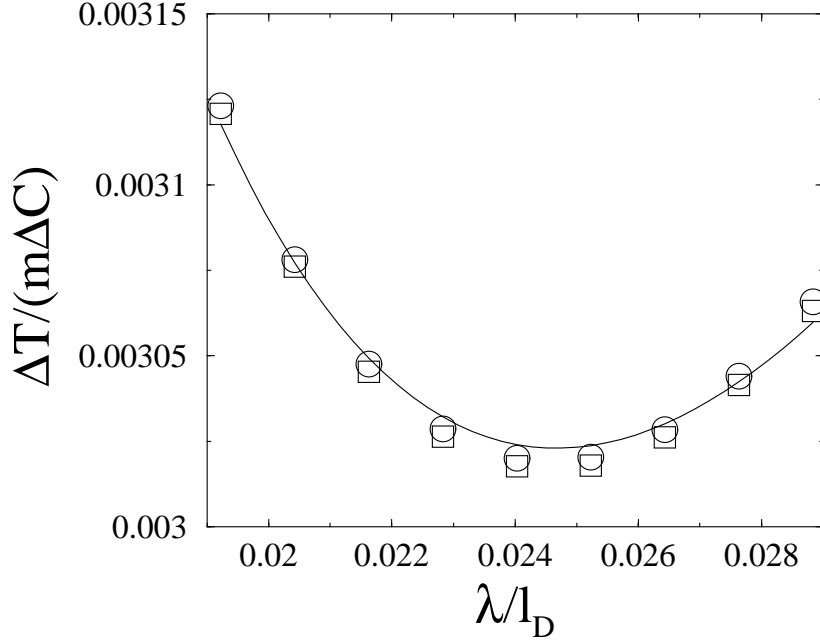
FIG. 12: Dimensionless average undercooling of the front versus dimensionless spacing ($l_D = D/v_p$ is the diffusion length) for the first two parameter sets of Table II. The curve is a best fit to the Jackson-Hunt law (see text for details).
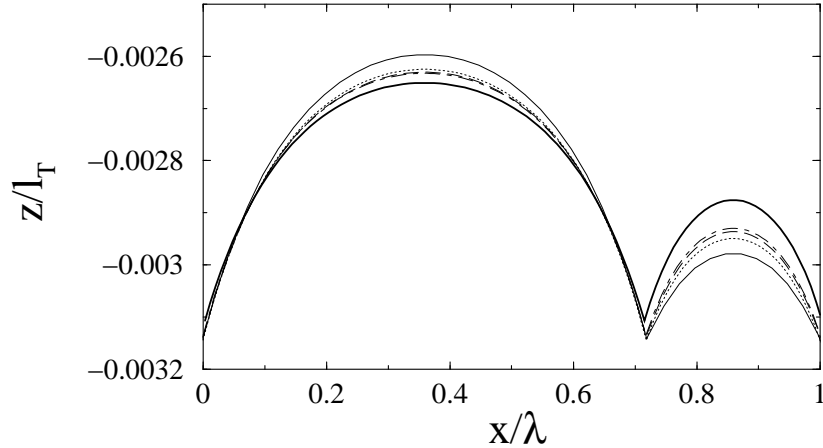
FIG. 13: Convergence test for lamellar shapes in CBr_4–C_2Cl_6. The parameters of all runs are given in Table III. Thin solid lines: $\lambda/W = 32$, dotted lines: $\lambda/W = 64$, dashed lines: $\lambda/W = 96$, dash-dotted lines: $\lambda/W = 128$; thick solid line: result of the boundary integral code of Ref. [17].

spacing is based on an approximate description of the front. We know from Fig. 10(a) that the difference in average undercooling between the phase-field model and the boundary-integral method is only 0.3 % near the minimum undercooling. Therefore, the 7 % difference with the Jackson–Hunt value must be attributed to the approximations in the theory, and not to the phase-field model.

Next, we repeat a similar procedure for the phase diagram of CBr_4–C_2Cl_6. The parameters are listed in Table. III, and the resulting interface shapes shown in Fig. 13. The behavior is qualitatively similar, but the convergence is slower. It can be seen that successive interface shapes fall closer and closer together as the resolution is increased. For the larger α lamella, the shape is converged for $\lambda/W \geq 64$; for the smaller β lamella, tiny differences remain visible even between 96 and 128. This is not surprising: convergence is harder to achieve when smaller physical details (such as the small β lamella here) must be resolved.

Again, the phase-field result is fairly close to the boundary integral calculation. However, this time a clearly visible
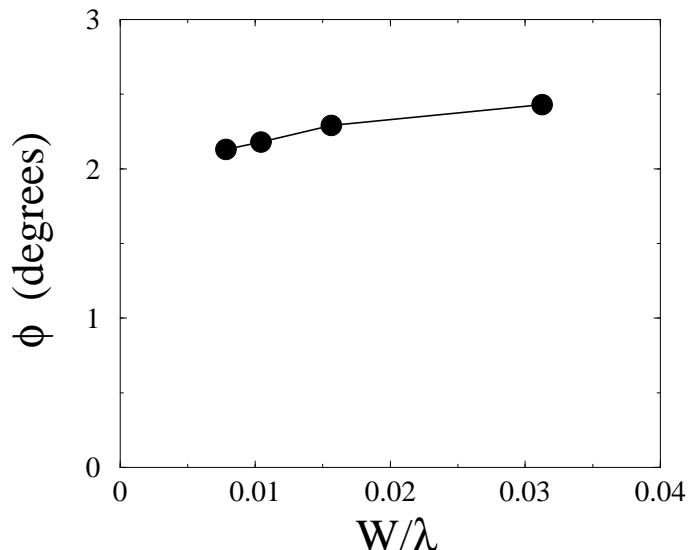
FIG. 14: Trijunction rotation angle ϕ (see text for definition) versus W/λ for the same series of runs as Fig. 13.

difference remains: Whereas the phase-field result is *above* the boundary integral for the α lamella, it is *below* for the β lamella. Therefore, the difference is not a simple shift between the two solutions. An explanation for this fact comes from the detailed examination of the angles at the trijunction point. Contrary to the completely symmetric situation where α and β are equivalent, the solid–solid interface does not remain straight up to the trijunction. Rather, when the trijunction is approached this interface starts to tilt and exhibits a small angle ϕ with the vertical axis. The angles between interfaces remain consistent with Young's law, but the whole trijunction zone is slightly rotated. Since we are in a steady state, the trijunction necessarily moves vertically (in the lab frame) as solidification proceeds. This implies that the solid–solid interface is not the mere trijunction trajectory, but must move after the trijunction passage, i.e., at its solid side, which is possible in a phase-field model, since the diffusivity decays to zero in the solid over a distance of order W. In the sharp-interface formulation, in contrast, where the diffusivity sharply falls to zero in the solid, the solid–solid interface cannot move and has to be strictly vertical up to the trijunction. This difference between phase-field model and sharp-interface description induces the observed shape difference between the converged phase-field solution and the boundary-integral result. We plot in Fig. 14 the rotation angle ϕ as a function of W/λ. Contrary to the deviation of the contact angle from its equilibrium value found in Fig. 11, this *global* trijunction rotation angle does *not* extrapolate to zero for $W/\lambda \to 0$, but rather seems to approach a finite value. This behavior will be discussed in more detail below.

E. Oscillatory limit cycles

As it is well known, lamellar steady-state growth becomes unstable above a critical spacing that depends on the growth conditions and the alloy composition. At the eutectic composition, the first instability to occur is a period-preserving oscillatory instability, that is, all lamellae of the same phase start to oscillate in phase. This instability can be captured by our reduced simulation geometry, because the center lines of each lamella remain symmetry planes of the pattern, whereas the time translation symmetry of steady-state growth is broken. The oscillations amplify in the course of time and finally saturate and reach a limit cycle with a well-defined amplitude. The bifurcation diagram of final oscillation amplitude versus lamellar spacing was found to be slightly supercritical in Ref. [17]. Simulating oscillatory limit cycles close to the instability threshold therefore constitutes a particularly sensitive test of our model, because even slight deviations in the lamellar spacing or differences in behavior will induce large changes in the oscillation amplitude.

We used the symmetric model alloy with the same physical parameters as in the preceding subsection, except the lamellar spacing, which was fixed to to $\lambda = 2.2 \, \lambda_{\mathrm{JH}}$. The simulations were started with a slightly asymmetric initial condition in which one of the lamellae was slightly ahead of the other. The limit cycle rapidly emerged; an example for the simulated structure once it has reached its final oscillation amplitude is shown in Fig. 15a for $\lambda/W = 64$. We define the amplitude A of the limit cycle as the maximum lateral deviation of the trijunction from its steady-state
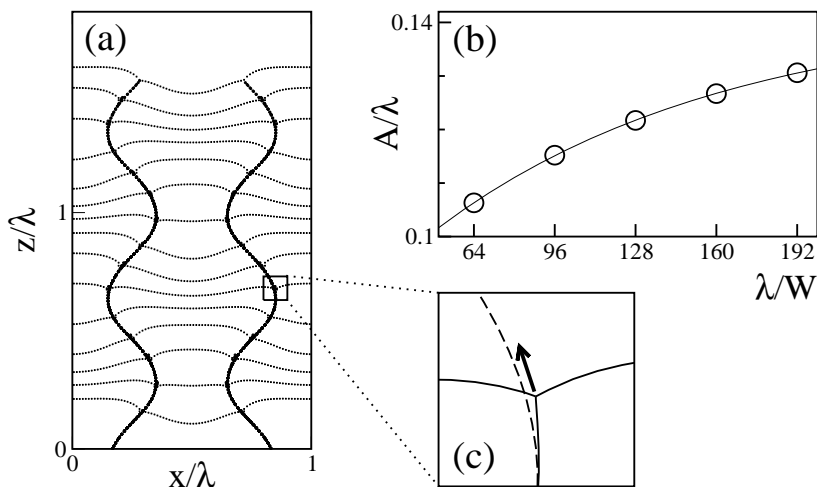
FIG. 15: Oscillatory limit cycle in the symmetric model alloy for $\lambda = 2.2\,\lambda_{\rm JH}$. (a) Snapshots of the two solid–solid interfaces (thick lines) and successive solid–liquid interfaces (thin lines). (b): Oscillation amplitude A/λ vs inverse interface thickness, λ/W. (c): Blowup of the trijunction region. The arrow in (c) indicates the direction of the trijunction motion.

value, normalized by the lamellar spacing, $A = \Delta x_{\rm max}/\lambda$. We plot A versus the resolution λ/W in Fig. 15b. It can be seen that the convergence is slow: the results still depend on the resolution even for $\lambda/W = 192$.

One possible reason for this slow convergence can be recognized in Fig. 15c, where we plot both a snapshot of a trijunction region (solid curves) and the final solid–solid interface left behind (dashed curve). Like for the asymmetric steady-state solutions, the trijunction seems to be slightly rotated, that is, the direction of the instantaneous solid–solid interface is not parallel to the direction of motion of the trijunction point (indicated in Fig. 15c by an arrow and roughly parallel to the final solid–solid interface).

Figure 15 seems to imply that our phase-field model commits large errors when calculating limit cycles. However, as already mentioned, we have chosen here a particularly sensitive test case. In Fig. 16, we show the whole bifurcation diagram, that is, the amplitude of saturated limit cycles versus the lamellar spacing, calculated with two different resolutions. As shown in the insets, the two curves can be superimposed quite nicely by a simple shift along the λ axis. Therefore, the relatively large difference in oscillation amplitudes comes from a small shift in the instability threshold, while the overall shape of the bifurcation diagram is quite robust. The relative error committed on the instability threshold is about 3 %. Hence, our model remains a useful tool for the exploration of nonlinear behavior in eutectic solidification, even if the trijunction behavior prevents completely converged calculations.

F.   Discussion

The most interesting outcome of the above numerical tests is the information about the behavior of trijunction points. As already mentioned, to our knowledge no detailed rigorous treatment of the equilibrium or dynamics of a diffuse trijunction is currently available, and it seems quite challenging indeed. Therefore, only a qualitative explanation of our numerical findings can be given, namely by comparing the phase-field and sharp-interface pictures.

In the sharp-interface model, Young's law is assumed to hold even outside of equilibrium; furthermore, the solid–solid interface cannot move, since the solute diffusivity vanishes in the solid immediately adjacent to the trijunction. In the phase-field simulations, both of these assumptions are relaxed. As for Young's law, there is a deviation from the equilibrium contact angles. In our simulations of the symmetric model alloy, this deviation decreases with the interface thickness and extrapolates to zero in the (numerical) sharp-interface limit. A likely origin of this effect is the relaxational time scale τ of the phase fields: A certain time is necessary to establish local equilibrium against the "pull" of the advancing isotherms.

A more surprising result is the rotation of the trijunction as a whole, which appears as soon as the symmetry between the two solid phases is broken. Here, we have shown only results at the eutectic composition for an asymmetric phase diagram; however, the same effect is recovered in the symmetric model alloy at off-eutectic composition, i.e., for unequal volume fractions of the two solids. The rotation does not seem to vanish when the interface width tends to zero. Although we cannot, at present, give a detailed explanation of this phenomenon, two speculative ideas about its origin might be pursued in the future. The first is that this effect could result from the local equilibrium of curved diffuse interfaces: Two different curvatures on the two sides of the trijunction could lead to some "torque" on the scale
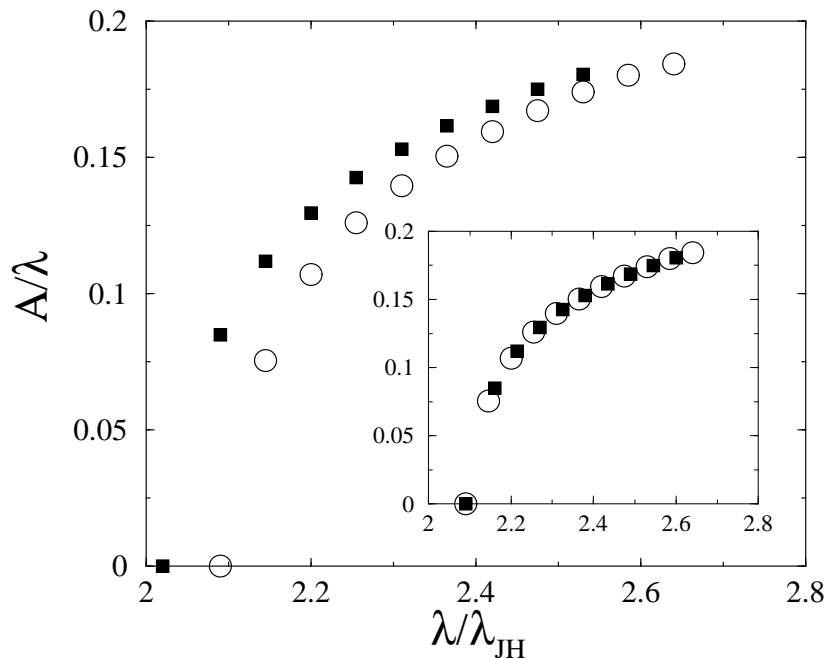
FIG. 16: Amplitude of saturated oscillatory limit cycles versus lamellar spacing, for parameters corresponding to the first (circles) and third (squares) lowest resolution in Fig. 15b ($\lambda/W = 64$ and 128 there, respectively). Inset: same data, where the squares have been shifted along the λ axis by 0.07.

of the diffuse trijunction. The second is that the solute diffusion field in the liquid "wedge" close to the trijunction yields a torque term *via* its coupling to the diffuse interfaces, which would be a purely non-equilibrium effect.

The origin of corrections to the classic sharp-interface model that do not vanish for sharp interfaces can be qualitatively understood. Contrary to the situation around a dendrite or cell tip, where the lower cutoff scale for the diffusion field is set by the local radius of curvature, a trijunction point is a singular point in the sharp-interface solution. Indeed, when the flux lines of the chemical components are drawn as sketched in Fig. 17, it can be seen that the curvature of these lines diverges as the trijunction point is approached. Therefore, the sharp-interface solution is, in some sense, inconsistent, because it is implicitly based on an assumption of scale separation between interface and "macroscopic" scales. Physical interfaces are smooth, and hence the local diffusion field around a trijunction varies *on the same scale as the interface thickness.* Therefore, the appearance of effects like the trijunction rotation is, in itself, not surprising. However, understanding them more quantitatively remains a challenging problem. More simulations are needed to study in detail the dependence of this phenomenon on the various parameters such as growth speed, contact angles, phase diagram and phase fractions.

Recently, the dynamics of trijunctions was found to have a noticeable influence on the stability of lamellar arrays at small spacings [28]. More precisely, the stability threshold for lamella elimination was found to be distinctly smaller than the minimum undercooling spacing, contrary to previous predictions [34, 35, 36]. The reason is that the assumption used in these predictions that trijunctions move in the direction normal to the large-scale envelope of the composite front (Cahn's rule) was not satisfied. It should be stressed that this effect is not necessarily related to the trijunction behavior found here, since Cahn's rule does not make any assumptions on the *local* configuration around a trijunction.

V.   CONCLUSIONS

We have presented and tested in detail a new phase-field model for two-phase solidification. The specific design of our free-energy functional has allowed us to clearly separate, at a local level, the dynamics of interfaces from those of trijunctions, and to eliminate all thin-interface corrections to the desired free-boundary dynamics for each solid–liquid interface. Both properties have been checked by numerical simulations: By the first we mean that interfaces between any two phases are completely free of the third phase far enough from the trijunctions, and this is indeed verified both at equilibrium and for moving interfaces (see Fig. 7). As for the second, it implies that simulations at fixed physical
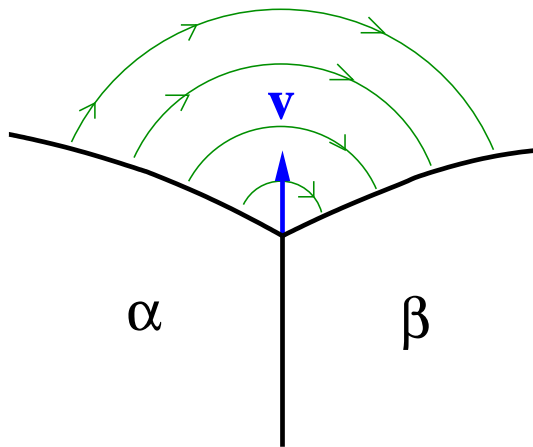
FIG. 17: Sketch of the diffusion field around a trijunction in the sharp-interface picture. Lines with arrows indicate the flux of solute around the trijunction. Sufficiently close to the trijunction, the concentration field obeys the Laplace equation, which is known to have a singularity in a wedge geometry.

parameters become independent of the interface thickness, provided that it is not too large. To our knowledge, it is the first time that the quantitative convergence to a sharp-interface solution as the interface thickness is decreased, as shown in Fig. 10, has been explicitly demonstrated for a phase-field model of solidification with more than one solid phase.

For generic, non-symmetric situations (unequal volume fractions or physical properties of the two solid-liquid equilibria), small differences exist between the converged phase-field results and boundary-integral simulations. Furthermore, while the convergence is very satisfying for steady-state solutions, time-dependent morphologies such as oscillatory limit cycles still exhibit thin-interface effects. Whereas these prevent us, for the moment, from achieving calculations that are completely independent of the computational parameters, we have demonstrated that the resulting errors are very small, except possibly in the vicinity of bifurcation points. Since our model is not only very accurate, but also efficient, it is a suitable tool for the investigation of pattern formation in two-phase solidification. In particular, it can be applied to simulate three-dimensional structures and to study their morphological stability [43].

Because the individual interface dynamics are perfectly distinct and controlled in our model, the only possible source of the observed differences to sharp-interface models lies in the trijunction region. Indeed, our detailed numerical investigation has revealed that the behavior of the diffuse trijunctions in the phase-field model differs slightly from the assumptions usually made in sharp-interface theories, as already discussed in Sec. IV F. Therefore, a quite surprising outcome of this study is that the calculation of two-phase microstructures is far more sensitive to the structure and dynamics of the trijunction points than one might have expected. Note that these findings have been possible only thanks to the specific design of our model, which has allowed us to eliminate all thin-interface corrections from the dynamics of the solid-liquid interfaces, and to separate them from those of the trijunctions. Therefore, our model is a privileged tool to explore in detail the physics of diffuse trijunctions, an interesting but challenging task. One conclusion of our study is that, apart from its undeniable fundamental interest, this more detailed knowledge is also a necessary ingredient for a future quantitative modeling of solidification with an arbitrary number of phases.

Let us conclude by sketching how our model can be extended to treat more general situations. Here, we have limited ourselves to eutectic diagrams with straight liquidus and solidus lines and constant concentration jumps; however, the structure of our model makes it possible to simulate any phase diagram. In particular, phase diagrams with curved coexistence lines as well as peritectic phase diagrams can be simulated without difficulty by choosing appropriate coefficients $A_i(T)$ and $B_i(T)$.

Next, because of our specific choice for the coupling between composition and phase fields, the model lacks the effect of the local interface curvature on the solute rejection. This (negligibly small) effect could be recovered by the introduction of more complicated interpolation functions, as shown for single-phase solidification in Ref. [8].

Furthermore, the asymptotic analysis and the antitrapping current in its present form are only applicable if the two solid–liquid surface tensions are equal. In order to keep the benefits of the model for arbitrary surface tensions, the asymptotic analysis should be repeated (in part numerically) along the lines of Ref. [8] as discussed in Sec. III H; this is a straightforward albeit tedious calculation.

We expect that crystalline anisotropy can be incorporated in the model in the standard way by making the interface thickness depend on the local orientation of the interfaces. However, care has to be taken in oder to ensure that the anisotropic model still has interfaces that are free of third-phase adsorption. Finally, some considerations on how to
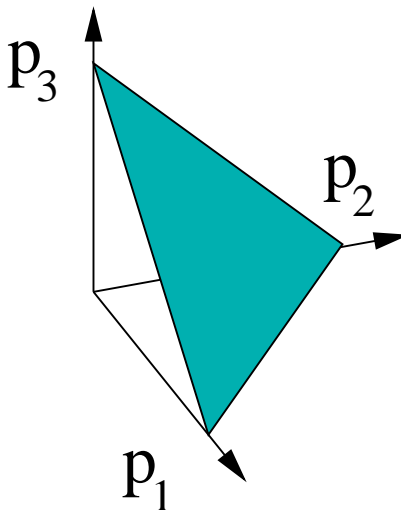
FIG. 18: Sketch of the phase-field state space. The representative point of the system is confined to the plane $p_1 + p_2 + p3 = 1$, whose intersection with the axes defines the vertices of the shadowed triangle, the so-called Gibbs simplex.

generalize the model to more than three phases are presented in appendix C.

APPENDIX A: TIME CONSTANTS

Here, we show that a linear relation between the time derivatives of the phase fields and the driving forces does not permit to choose different relaxation times for different interfaces and still guarantee that each interface is free of any third phase.

A given configuration of the phase fields can be visualized by a representative point in the three-dimensional vector space spanned by the axes p_1, p_2 and p_3 (see figure 18). The constraint $p_1 + p_2 + p_3 = 1$ restricts the allowed positions to a two-dimensional subspace, the plane that contains the points $(1, 0, 0)$, $(0, 1, 0)$, and $(0, 0, 1)$. These points are also the vertices of an equilateral triangle, the Gibbs simplex (shadowed area). Only points inside the triangle (shadowed area) are meaningful if each phase field is to be interpreted as a *positive* volume fraction.

The most general form for a linear relationship between the time derivatives of the phase fields and the driving forces $\delta F / \delta p_i$ is

$$\frac{\partial p_i}{\partial t} = -\sum_{j=1}^{3} \Gamma_{ij} \frac{\delta F}{\delta p_j}, \tag{A1}$$

where Γ_{ij} can be seen as a linear map between the vector of the driving forces, $\delta F / \delta p_i$, and the vector of the time derivatives, $\partial p_i / \partial t$. Since the representative point must remain in the plane which contains the Gibbs simplex, the vector of the time derivatives must also lie in it, and therefore be normal to the vector $(1, 1, 1)$. In contrast, there are no explicit constraints on the vector of the driving forces, which can have any direction. Therefore, the matrix Γ_{ij} must have the eigenvector $(1, 1, 1)$ with eigenvalue zero, or, in other words, be a projection on the allowed plane.

In addition, the free-energy density F is designed so that on purely binary interfaces there is no driving force for the formation of the third phase. For example, on the 1-2-interface, the driving force along the p_3-direction is zero; therefore, the vector $\delta F / \delta p_i$ is parallel to $(1, -1, 0)$. Since we do not want the resulting time evolution to introduce the third phase, the vector of the time derivatives must also be parallel to $(1, -1, 0)$. This implies that this vector must be an eigenvector of the matrix Γ_{ij}. The corresponding eigenvalue is the relaxation rate for the 1-2-interface.

The same reasoning can be repeated for the 1-3-interface, with the associated eigenvector $(1, 0, -1)$. Since the two vectors are not orthogonal, the only possibility that makes both of them eigenvectors is that the whole subspace corresponding to the plane of the Gibbs simplex is an eigenspace with a single eigenvalue. Therefore, all the time constants associated with purely binary interfaces are the same, and the only valid choice for the matrix Γ is a multiple of the projector on the plane of the simplex,

$$\Gamma_{ij} = \Gamma\left(\delta_{ij} - u_i u_j\right) \tag{A2}$$

where $\hat{u} = (1, 1, 1)/\sqrt{3}$ is the unit vector normal to the simplex plane. Writing $\Gamma = 1/(\tau H)$, the resulting equations of motion are

$$\tau \frac{\partial p_i}{\partial t} = -\frac{1}{H} \sum_{j=1}^{3} \left(\delta_{ij} - \frac{1}{3}\right) \frac{\delta F}{\delta p_j}. \tag{A3}$$

This is equivalent to Eqs. (3.4) in conjuction with the prescription of Eq. (3.5).

The only way to achieve different relaxation times for the different interfaces while keeping purely binary interfaces is therefore to introduce some nonlinearity in the relation between time derivatives and driving forces. We achieve this by letting the time constant τ depend on the phase fields. Note that locally "anisotropic" dynamics in the configuration space could also be induced by letting all the coefficients Γ_{ij} depend on the phase fields, so that the directions of the eigenvectors and the associated eigenvalues depend on the location in the configuration space.

APPENDIX B: SYMMETRY OF THE GRADIENT ENERGY COEFFICIENTS

The gradient energy expression, Eq. (3.11), satisfies the conditions for no third-phase adsorption, Eqs. (3.9). We now consider its simplest generalization,

$$f_{\mathrm{grad}} = \sum_{mn} \frac{\xi_{mn}}{2} \vec{\nabla} p_m \cdot \vec{\nabla} p_n, \tag{B1}$$

a quadratic form in the gradients of the phase fields, where the ξ_{mn} are dimensionless constants that we assume to be symmetric (and positive), $\xi_{mn} = \xi_{nm}(> 0)\ \forall m, n$. We find that Eq. (3.9a) is satisfied if and only if the coefficients that multiply the Laplacians of the phase fields in each purely binary interface are all the same, so that this generalization does not provide any extra freedom for our purposes.

To see this, compute the functional, constrained derivatives of a free-energy functional F_{grad} defined as the volume integral of the gradient terms alone, $F_{\mathrm{grad}} = \int_V K f_{\mathrm{grad}}$. Making use of Eqs. (3.5) and (3.6), we find

$$-\frac{\delta F_{\mathrm{grad}}}{\delta p_k}\bigg|_{p_\alpha + p_\beta + p_{\mathrm{L}} = 1} = K\left(\sum_m \xi_{mk} \vec{\nabla}^2 p_m - \frac{1}{3}\sum_{mn} \xi_{mn} \vec{\nabla}^2 p_m\right). \tag{B2}$$

The condition of flatness with respect to variations of p_k on a i–j interface, Eq. (3.9a), then yields

$$\xi_{ii} - 2\xi_{ik} = \xi_{jj} - 2\xi_{jk}, \tag{B3}$$

where we have taken into account that $p_k \equiv 0$ and $p_j = 1 - p_i$. This can be written in a more symmetric way by adding ξ_{kk} to both sides:

$$\xi_{kk} - 2\xi_{ik} + \xi_{ii} = \xi_{kk} - 2\xi_{jk} + \xi_{jj}. \tag{B4}$$

Two equivalent conditions can be obtained for the other two interfaces, so that all three symmetric combinations $\xi_{mm} - 2\xi_{mn} + \xi_{nn}$ must have the same value.

Next, replace k with i in Eq. (B2) and, afterwards, apply it to a i–j interface ($p_k = 0$). One finds

$$-\frac{\delta F_{\mathrm{grad}}}{\delta p_i}\bigg|_{p_\alpha + p_\beta + p_{\mathrm{L}} = 1} = \frac{K}{3}(2\xi_{ii} + \xi_{jj} - 3\xi_{ij} - \xi_{ik} + \xi_{jk})\nabla^2 p_i. \tag{B5}$$

Using Eq. (B3) to eliminate $\xi_{jk} - \xi_{ik}$, we find that the prefactor of the Laplacian can be rewritten as $(K/2)(\xi_{ii} - 2\xi_{ij} + \xi_{jj})$, i.e., one half of the combination that we saw above to be the same for all interfaces. Therefore, we can choose $\xi_{ij} = \delta_{ij}$ without loss of generality, and we are back to the minimal model with Eq. (3.11).

The multi-phase-field models based on the approach of Steinbach et al. [22] use a different expression for the gradient terms. It combines gradients of the phase fields with the fields itself, and is hence not a simple quadratic form in the gradients. We have checked that this expression does not satisfy the condition of flatness; therefore, it is not a suitable alternative for our purposes.

APPENDIX C: MORE THAN THREE PHASES

In principle, the multi-phase formalism where each phase field represents a local volume fraction can be extended to an arbitrary number of phases. However, the methods we have applied to ensure that interfaces are free of any adsorbed third phase need to be generalized with care. Let us consider a multi-well potential f_{MW} constructed in the same manner as our triple-well potential f_{TW}, i.e., by a superposition of individual double-well potentials for each phase field, $f_{\mathrm{MW}} = \sum_i f_{\mathrm{DW}}(p_i)$. For $f_{\mathrm{DW}}(p) = |p|^v |1-p|^v$ (with v a positive real) the free energy of a point where n phases coexist (n-junction) is $n^{1-2v}(n-1)^v$. For our model, $v = 2$, this expression has a single maximum at $n = 3$. Therefore, a quadrijunction already has a lower free energy than a trijunction, which means that the free-energy landscape f_{MW} has undesirable local minima for more than three phases. These lower-energy n-junctions can always be "raised" by adding one obstacle term $f_{\mathrm{obs}} = \Pi_{i=1}^n p_i^2$ per n-junction to treat. However, the number of such terms becomes rapidly prohibitive when n increases; in addition, such "steep" terms require a higher numerical resolution. Alternatively, for $0 < v \leq 1$ the n-junction energy becomes monotonously increasing in n for all positive n. Therefore, the simplest choice ensuring the right topography for an arbitrary number of phases would be $v = 1$, a model considered in Ref. [31]; however, to our knowledge no thin-interface analysis has been performed to date for this inverse parabolic potential.

---

[1] W. J. Boettinger, J. A. Warren, C. Beckermann and A. Karma, Annu. Rev. Mater. Res. **32**, 163 (2002).
[2] L.-Q. Chen, Annu. Rev. Mater. Res. **32**, 113 (2002).
[3] D. M. Anderson, G. B. McFadden and A. A. Wheeler, Ann. Rev. Fluid Mech. **30**, 139 (1998).
[4] R. Folch, J. Casademunt, A. Hernández-Machado and L. Ramírez-Piscina, Phys. Rev. E **60**, 1724 (1999); *ibid.* **60**, 1734 (1999).
[5] D. A. Kessler, J. Koplik and H. Levine, Adv. Phys. **35**, 255 (1988); P. Pelcé, *Dynamics of Curved Fronts* (Academic Press, New York, 1988).
[6] P. C. Hohenberg and B. I. Halperin, Rev. Mod. Phys. **49**, 435 (1977).
[7] A. Karma and W.-J. Rappel, Phys. Rev. E **53**, R3017 (1996); ibid. **57**, 4323 (1998).
[8] A. Karma, Phys. Rev. Lett. **87**, 115701 (2001); B. Echebarria, R. Folch, A. Karma, and M. Plapp, Phys. Rev. E **70**, 061604 (2004).
[9] A. Karma and W.-J. Rappel, Phys. Rev. Lett. **77**, 4050 (1996); M. Plapp and A. Karma, Phys. Rev. Lett. **84**, 1740 (2000); A. Karma, Y. H. Lee, and M. Plapp, Phys. Rev. E **61**, 3996 (2000).
[10] W. Kurz and D. J. Fisher, *Fundamentals of Solidification* (Trans Tech, Aedermannsdorf, Switzerland, 1992).
[11] J. D. Hunt and K. A. Jackson, Trans. AIME **236**, 843 (1966).
[12] V. Seetharaman and R. Trivedi, Met. Trans. A **19**, 295 (1988).
[13] G. Faivre and J. Mergy, Phys. Rev. A **45**, 7320 (1992).
[14] M. Ginibre, S. Akamatsu, and G. Faivre, Phys. Rev. E **56**, 780 (1997).
[15] S. Akamatsu, S. Moulinet, and G. Faivre, Met. Mat. Trans. A **32**, 2039 (2001).
[16] K. Kassner and C. Misbah, Phys. Rev. A **44**, 6513 (1991).
[17] A. Karma and A. Sarkissian, Met. Trans. A **27**, 635 (1996).
[18] A. Karma, Phys. Rev. E **49**, 2245 (1994).
[19] K. R. Elder, F. Drolet, J. M. Kosterlitz, and M. Grant, Phys. Rev. Lett. **72**, 677 (1994).
[20] A. A. Wheeler, G. B. McFadden, and W. J. Boettinger, Proc. R. Soc. London, Ser. A **452**, 495 (1996).
[21] T. S. Lo, A. Karma, and M. Plapp, Phys. Rev. E **63**, 031504 (2001).
[22] I. Steinbach, F. Pezzolla, B. Nestler, M. Seeßelberg, R. Prieler, G. J. Schmitz, and J. L. L. Rezende, Physica D **94**, 135 (1996).
[23] J. Tiaden, B. Nestler, H.-J. Diepers, and I. Steinbach, Physica D **115**, 73 (1998).
[24] B. Nestler and A. A. Wheeler, Physica D **138**, 114 (2000).
[25] M. Plapp and A. Karma, Phys. Rev. E **66**, 061608 (2002).
[26] R. Folch and M. Plapp, pp. 182–189 in *Interface and Transport Dynamics – Computational Modelling*, edited by H. Emmerich, B. Nestler, and M. Schreckenberg, Lecture Notes in Computational Science and Engineering **32** (Springer, Berlin, 2003); see also cond-mat/0206237.
[27] S. G. Kim, W. T. Kim, T. Suzuki, and M. Ode, J. Cryst. Growth **261**, 135 (2004).
[28] S. Akamatsu, M. Plapp, G. Faivre, and A. Karma, Phys. Rev. E **66**, 030501(R) (2002); Met. Mat. Trans. A **35**, 1815 (2004).
[29] J. F. Blowey and C. M. Elliott, in *Proceedings of the IMA Workshop*, IMA Volumes in Mathematics and its Applications **47**, edited by W.-M. Ni, L. A. Peletier, and J. L. Vazquez (Springer, New York, 1993).
[30] H. Garcke, B. Nestler, and B. Stoth, SIAM J. Appl. Math. **60**, 295 (1999).
[31] I. Steinbach and F. Pezzolla, Physica D **134**, 385 (1999).
[32] R. Folch and M. Plapp, Phys. Rev. E **68**, 010602(R) (2003).
[33] J. Mergy, Ph. D. thesis, University Paris VII (1992).

[34] J. S. Langer, Phys. Rev. Lett. **44**, 1023 (1980).

[35] V. Datye and J. S. Langer, Phys. Rev. B **24**, 4155 (1981).

[36] K. A. Jackson and J. D. Hunt, Trans. AIME **236**, 1129 (1966).

[37] R. F. Almgren, SIAM J. Appl. Math **59**, 2086 (1999).

[38] This is the main difference to the first version of our model published in [26].

[39] The same evolution equations on an i–j interface can be obtained by taking the functional derivative of the free energy evaluated on that interface with respect to either of the non-vanishing phase fields. This is possible thanks to the fact that the derivatives normal to that interface vanish, so that the operators corresponding to setting $p_k = 0$ and taking the functional derivative commute. However, by this method, since one eliminates p_j in terms of p_i before taking the derivative with respect to p_i, the contribution of p_i is double-counted, so that the result needs to be divided by two.

[40] The values of the constants a_1 and a_2 are related to those calculated by Karma and Rappel in Ref. [7] and denoted here by a_1^{KR} and a_2^{KR}, by $a_1 = (8/15)a_1^{KR}$ and $a_2 = (15/8)a_2^{KR}$.

[41] M. Plapp and A. Karma, J. Comput. Phys. **165**, 592 (2000).

[42] Note that the partition relation, Eq. (2.3), has to be replaced by $C_- = C_+ - (C_L - C_i)$ when $k_i \to 1$.

[43] M. Dejmek, R. Folch, A. Parisi, and M. Plapp, in *Solidification processes and microstructures: A symposium in honor of Prof. W. Kurz*, edited by M. Rappaz, C. Beckermann, and R. Trivedi, The Minerals, Metals and Materials Society (Warrendale, PA, 2004); see also cond-mat/0401250.